

## Probing Feedback via IGM tomography and Ly $\alpha$ forest with Subaru PFS, TMT/ELT, & JWST

KENTARO NAGAMINE,<sup>1,2,3</sup> IKKOH SHIMIZU,<sup>4</sup> KATSUMI FUJITA,<sup>1</sup> NAO SUZUKI,<sup>2</sup> KHEE-GAN LEE,<sup>2</sup> RIEKO MOMOSE,<sup>5</sup> SHIRO MUKAE,<sup>6,5</sup> YONGMING LIANG,<sup>5,7</sup> NOBUNARI KASHIKAWA,<sup>5</sup> MASAMI OUCHI,<sup>7,5,6</sup> AND JOHN D. SILVERMAN<sup>2</sup>

<sup>1</sup>*Theoretical Astrophysics, Department of Earth and Space Science, Graduate School of Science, Osaka University, 1-1 Machikaneyama, Toyonaka, Osaka 560-0043, Japan*

<sup>2</sup>*Kavli-IPMU (WPI), University of Tokyo, 5-1-5 Kashiwanoha, Kashiwa, Chiba, 277-8583, Japan*

<sup>3</sup>*Department of Physics & Astronomy, University of Nevada, Las Vegas, 4505 S. Maryland Pkwy, Las Vegas, NV 89154-4002, USA*

<sup>4</sup>*Shikoku Gakuin University, 3-2-1 Bunkyocho, Zentsuji, Kagawa, 765-8505, Japan*

<sup>5</sup>*Department of Astronomy, University of Tokyo, 7-3-1 Hongo, Bunkyo, Tokyo, 113-8654, Japan*

<sup>6</sup>*ICRR, University of Tokyo, 5-1-5 Kashiwanoha, Kashiwa, Chiba, 277-8582, Japan*

<sup>7</sup>*National Astronomical Observatory of Japan, Mitaka, Tokyo, Japan*

### ABSTRACT

In preparation for the IGM tomography study by Subaru Prime Focus Spectrograph (PFS) survey and other large future telescopes such as TMT/ELT/GMT, we present the results of our pilot study on Lyman- $\alpha$  forest and IGM tomography statistics using the GADGET3-OSAKA cosmological smoothed particle hydrodynamical simulation. Our simulation includes models for star formation and supernova feedback, which enables more realistic cross-correlation studies between galaxies, neutral hydrogen (HI) and metals in circumgalactic and intergalactic medium. We create light-cone data set at  $z = 2 - 3$  from our simulations and generate mock Ly $\alpha$  forest data. As a first step, in this paper, we focus on the distribution of HI and galaxies, and present statistical results on 1-D flux PDF, 1-D power spectrum, flux contrast vs. impact parameter, HI-galaxy cross-correlations. Our results show overall agreement with current observational data, with some interesting discrepancies on small scales which are due to either feedback effects or varying observational conditions. Our simulation shows stronger HI absorption with decreasing transverse distance from galaxies. We find that the massive galaxies with  $M_{\star} \geq 10^{10} M_{\odot}$  contribute strongly to the flux contrast signal, and that the lower mass galaxies with  $M_{\star} \sim 10^8 - 10^{10} M_{\odot}$  tend to dilute the flux contrast signal from massive galaxies. On large scales, the average flux contrast smoothly connects to the IGM level, supporting the concordance  $\Lambda$  cold dark matter model. We also find an increase in the HI absorption towards the center of a proto-cluster.

*Keywords:* cosmology — intergalactic medium — neutral hydrogen — galaxy formation — numerical simulation

### 1. INTRODUCTION

Understanding the distribution of baryons and galaxies is one of the most important topics in modern cosmological studies. In particular, hydrogen is the most abundant element in our Universe, and the distribution of neutral hydrogen (HI) contains useful information on the radiative history of our Universe, e.g., evolution of the ultra-violet background (UVB) radiation field, cosmic star formation history, and the interaction between galaxies, circum-galactic medium (CGM; e.g., Tumlin-

son et al. 2017) and inter-galactic medium (IGM; e.g., Meiksin 2009; McQuinn 2016).

The HI gas at cosmological distances can be observed as Lyman- $\alpha$  (hereafter Ly $\alpha$ ) forest in quasar absorption lines, and abundant data from high-resolution spectroscopy has been collected over the past few decades (e.g., Weymann et al. 1981; Cowie et al. 1995; Rauch 1998). In conjunction with those observational efforts, cosmological hydrodynamic simulations have played crucial roles in deepening our understanding of the nature of Ly $\alpha$  forest clouds (Cen et al. 1994; Hernquist et al. 1996; Miralda-Escudé et al. 1996; Zhang et al. 1997, 1998), and it is generally accepted that the Ly $\alpha$  forest originates from the diffuse HI gas in filamentary structures

as well as the gaseous clouds mildly bound by gravity (Ly-limit systems). The Ly $\alpha$  forest has proven to be one of the most powerful probes of cosmology, and it has been used to constrain the cosmological parameters (Weinberg et al. 1998b; McDonald et al. 2006), the matter power spectrum (Croft et al. 1998; Iršič et al. 2017), the mass of warm dark matter particles (e.g. Viel et al. 2005, 2013a), the mass of neutrinos (Palanque-DeLabrouille et al. 2015), and the impact of supernova feedback on IGM (e.g. Theuns et al. 2002; Cen et al. 2005; Kollmeier et al. 2006).

Over the past several years, by utilizing a large quasar catalogue from the Sloan Digital Sky Survey (SDSS-BOSS; Dawson et al. 2013,  $\sim 160,000$  sight lines), significant HI overdensities (i.e. proto-cluster candidates) have been identified at  $z = 2 - 3$  (Cai et al. 2016, 2017; Mukae et al. 2020; Ravoux et al. 2020), which are expected to be a more uniform, unbiased sample of proto-clusters, covering a large cosmological volume of  $\sim \text{Gpc}^3$ . (However, note the cautionary remarks by Miller et al. 2019 as well. See also Section 3.6 for related discussions.) These proto-clusters will serve as unique test beds for the hierarchical structure formation scenario (Overzier 2016; Chiang et al. 2017). For example, the most massive galaxies are found in proto-clusters, and they are expected to be the first ones to make transition from the star-forming blue sequence to the red sequence. The connections between radio galaxies, Ly $\alpha$  blobs and proto-clusters are also of significant interest (e.g., Umemoto et al. 2015, 2020).

One can also perform the ‘IGM tomography’ using more ubiquitous bright star-forming galaxies (e.g., Ly-break galaxies [LBGs] at  $z \sim 3$ ) as background sources, and measure the 3D distribution of HI gas in the foreground at  $z = 2 - 3$ . Indeed, Lee et al. (2014) have demonstrated that this can be done using the Keck telescope, i.e., the CLAMATO survey (Lee et al. 2018). A galaxy proto-cluster has been identified at  $z = 2.44$  by the Ly $\alpha$  tomographic technique (Lee et al. 2016). The scientific goals of IGM tomography are: (i) to characterize the cosmic web at  $z > 2$ , (ii) to study the association between galaxies/AGN and HI gas, and (iii) to identify proto-clusters and voids in an unbiased fashion.

There are many large spectroscopic surveys being planned in the next decade to probe intermediate redshift range of  $z > 1$ . The Sloan Digital Sky Survey (SDSS) and 2-degree Field (2dF) surveys gave us excellent views of our local Universe, and the ‘SDSS at  $z \sim 1$ ’ will soon become available by the combination of Subaru Hyper-Supreme Cam (HSC) and Prime Focus Spectrograph (PFS) projects (Takada et al. 2014). The Subaru PFS survey is a large spectroscopic survey

on the Subaru telescope employing  $\sim 2400$  fibers positioned across a 1.3 deg field, which is scheduled to start from  $\sim 2022$ . It follows up on the ongoing HSC imaging survey, and the combination of the two large projects will present unique opportunities to study galaxy evolution and HI distribution in our Universe at the same time. The high- $z$  program of the PFS project plans to cover the sky area of 15 deg $^2$  of the HSC deep fields, and is likely to include topics such as the IGM tomography at  $z = 2 - 3$ , galaxy evolution at  $z = 2 - 6$ , reionization studies using Ly $\alpha$  emitters (LAEs) at  $z = 6 - 7$ .

While there are other similar projects to the Subaru PFS utilizing multiplexed fiber spectrograph, such as the WEAVE (Dalton et al. 2012) and the MOONS (Cirasuolo et al. 2014), PFS has a unique combination of both telescope diameter and spectral coverage into the blue. This allows it to observe large numbers of galaxies at  $z \sim 2 - 3$  and at the same time measure the Ly $\alpha$  forest absorption with large numbers of background sources.

In this paper, we focus on the science cases related to the PFS IGM tomography program, and prepare to make some forecasts using cosmological hydrodynamic simulations that include full physics of star formation and supernova (SN) feedback. Some details of the Subaru PFS project is summarized in Appendix A.

For the IGM tomography, the spatial resolution of current observational study is still coarse, and numerical simulations can provide useful comparison data set, by mimicing the actual observations to evaluate the expected observational results. For example, Lukić et al. (2015) used the NYX hydrodynamic simulation to examine Ly $\alpha$  forest statistics, but without generating full light-cone dataset nor the treatment of star formation and feedback (i.e., an optically-thin calculation). They found that the hydrodynamic resolution of  $20 h^{-1} \text{kpc}$  is required to achieve 1 per cent convergence of Ly $\alpha$  forest flux statistics up to  $k = 10 h \text{Mpc}^{-1}$ , and box sizes of  $L > 40 h^{-1} \text{cMpc}$  is needed to suppress the errors to sub-percent level for the 1D flux power spectrum. Typically, convergence of 5 – 10 per cent had been reported by several authors using box sizes of  $20 - 40 h^{-1} \text{cMpc}$  with resolutions of  $50 - 200 h^{-1} \text{ckpc}$  at  $z \sim 2$  (e.g. Meiksin & White 2004; McDonald et al. 2005; Viel et al. 2006; Bolton & Becker 2009; Tytler et al. 2009; Meiksin et al. 2014).

Furthermore, Sorini et al. (2018) used the Illustris and NYX simulations to examine the average Ly $\alpha$  absorption profile around galaxies, and showed that the results agree well with the observations by BOSS (Font-Ribera et al. 2013) and quasar pairs (Prochaska et al. 2013; Rubin et al. 2015) at transverse distances of  $2 \lesssim b \lesssim 20 \text{Mpc}$ . They argued that the nice asymptotic agree-

ment of the absorption profile on large scales is a reflection of the fact that the  $\Lambda$ CDM model successfully describes the distribution of ambient IGM around the dark matter halos. Based on the comparison between the simulations and observations, they also suggested that the ‘sphere of influence’ of galaxies could extend out to  $\sim 7$  times the halo virial radius, i.e. to  $\sim 2$  Mpc, and that there are significant differences between the simulations and observations on small scales of  $\lesssim 100$  kpc. The earlier similar works using hydrodynamic simulations include e.g., Bruscoli et al. (2003); Kollmeier et al. (2003, 2006); Meiksin et al. (2015, 2017). Sorini et al. (2018) also showed that the both Illustris and NYX simulations underpredict the Ly $\alpha$  absorption profile around quasars and LBGs at small separations of  $b < R_{\text{vir}}$ . Sorini et al. (2020) further examined the SIMBA hydrodynamic simulation and showed that it overpredicts the absorption (i.e. flux contrast) on small scales of  $b < 100$  kpc significantly. We show in this paper that our GADGET3-OSAKA simulation does not have these problems on small scales, and we highlight the variation caused by the differences in feedback models and galaxy samples.

An important difference of the present work over the earlier ones which adopted optically-thin fluctuating Gunn-Peterson approximation (FGPA) treatment (Weinberg et al. 1998b; Croft et al. 1998) or those without detailed treatment of star formation and feedback, is that we use cosmological hydrodynamic simulations with detailed models of star formation and SN feedback (but no AGN feedback yet). For example, the SHERWOOD simulations (Bolton et al. 2017) operate at slightly higher resolution than our simulation, but they did not treat the star formation and metal enrichment process in detail, and instead resorted to a simplified model of converting the highest density gas into star particles to save computing time (see also Meiksin et al. 2014, 2015, 2017).

We note that Sorini et al. (2020) found that the impact of AGN feedback is not so strong, and that the stellar feedback is the primary driver for determining the average physical properties of CGM at  $z = 2 - 3$ . Their claim needs to be checked in other simulations with AGN feedback in the future, but the absence of AGN feedback treatment in the present paper is perhaps not so critical, as we are not discussing the proximity effect around quasars in particular (but see the discussion in Section 3.6).

As a pathfinder to the IGM tomography studies by the Subaru PFS and upcoming large telescopes such as TMT/ELT, we examine various statistics related to the Ly $\alpha$  forest, such as the 1D flux PDF, 1D power

spectrum, Ly $\alpha$  decrement as a function of transverse distance from galaxies, and cross-correlation between galaxies and HI gas. This is only our first step towards more rigorous comparisons between simulations and observations of CGM & IGM. In this paper, we focus on the relative distribution of galaxies and HI, and do not touch on the metal absorption lines, which we will discuss in our later publications. The goal of this paper is not to argue for a best-fit simulation parameter set or subgrid models, but rather to highlight the differences with the currently available observational data and look for the right directions for our future research. The astrophysics in this subject is quite rich, as we need to have a good understanding of cosmology, galaxy formation, star formation, feedback and chemical enrichment of the IGM, and link them all together to have a full picture.

The results presented in this paper serve as the basis of our future work of comparing the simulations and observations, for example, as presented by Momose et al. (2020, 2021); Liang et al. (2021). We will refer to these results in more detail in later sections.

This paper is organized as follows. We describe the details of our cosmological hydrodynamic simulations in Section 2.1, and the method of generating the Ly $\alpha$  forest data is presented in Section 2.2. In Section 3, we lay out the results of Ly $\alpha$  flux PDF, 1D Ly $\alpha$  power spectrum, flux contrast vs. impact parameter from galaxies, cross-correlation between galaxies and HI, correlation between galaxy overdensity and Ly $\alpha$  absorption decrement, and finally the flux contrast in a proto-cluster. We then present our discussion and summary in Section 4.

## 2. SIMULATIONS AND METHODS

### 2.1. Cosmological Hydrodynamic Simulations

We use the GADGET3-OSAKA cosmological smoothed particle hydrodynamics (SPH) code (Aoyama et al. 2017; Shimizu et al. 2019), which is a modified version of GADGET-3 (originally described in Springel 2005, as GADGET-2). Our code includes important improvements such as the density-independent, pressure-entropy formulation of SPH (Hopkins 2013; Saitoh & Makino 2013), the time-step limiter (Saitoh & Makino 2009), and quintic spline kernel (Morris 1996).

Our code also includes models for star formation and SN feedback. We adopt the basic model of star formation in the AGORA project (Kim et al. 2014, 2016). The SN feedback recipe is described in detail by Shimizu et al. (2019), which we briefly summarize here. The feedback energy and metals are deposited within a hot bubble radius computed from a Sedov-Taylor-like solution which takes the cooling into account (Chevalier 1974;

McKee & Ostriker 1977), similarly to the blast-wave model by Stinson et al. (2006). We also use the CELib chemical evolution library by Saitoh (2017) and appropriate time delays for Type Ia & II SNe, and AGB stars. The energy and metals are injected into the surrounding ISM with appropriate time delays for different sources based on CELib, following each star formation event. We compute the total feedback energy for each star-forming event, and deposit both thermal (70%) and kinetic (30%) energy to the neighboring gas particle within the hot bubble radius, as in the fiducial model of Shimizu et al. (2019). Through the tests with isolated AGORA galaxies, we have found that this fiducial model has a moderate degree of chemical enrichment without overheating the IGM, unlike the original constant wind velocity model by Springel & Hernquist (2003). The merit of the Osaka feedback model is that the wind velocity and the hot bubble size is determined based on the local physical quantities (gas density, pressure, available feedback energy) rather than the bulk quantities such as galaxy stellar mass or halo mass, and this is more favorable for future higher resolution simulations.

The uniform UV radiation background model of Haardt & Madau (2012) is adopted. In one of the simulation runs, the self-shielding by optically-thick gas is treated following the prescription of Rahmati et al. (2013, which is based on the earlier similar works by Nagamine et al. 2010; Altay et al. 2011; Yajima et al. 2012; Bird et al. 2013) to test its impact on the Ly $\alpha$  forest statistics. The cooling is solved by the Grackle chemistry and cooling library (Smith et al. 2017)<sup>1</sup> with the option of ‘`primordial_chemistry=3`’ which computes the detailed non-equilibrium chemistry network of twelve species. Metal line cooling is also solved.

In this paper, we primarily use cosmological hydrodynamic simulations with a box size of  $100 h^{-1}\text{Mpc}$  (comoving; hereafter cMpc) with total initial particle number of  $2 \times 512^3$ . We also use another simulation with a box size of  $50 h^{-1}\text{cMpc}$  and  $2 \times 256^3$  particles to examine the box-size effect, but the results are very similar and we do not show the comparison here. Given the above parameters, the two simulations have exactly the same mass/spatial resolution, however, the  $50 h^{-1}\text{cMpc}$  box is slightly too small to create the light-cone data set for the Ly $\alpha$  forest study at  $z \approx 2 - 3$ . We find that we have sufficient resolution to resolve the Ly $\alpha$  forest in the wavelength space compared to the observations as we demonstrate later. The initial particle masses in the two simulations are  $1.00 \times 10^8 h^{-1}\text{M}_\odot$  and

**Table 1.** List of Numerical Simulations

Model	Notes
Osaka20-Fiducial	no self-shielding
Osaka20-Shield	with self-shielding
Osaka20-NoFB	no SN feedback
Osaka20-CW	Constant velocity galactic wind model <sup>a</sup>
Osaka20-FG09	UVB model of FG09 <sup>b</sup>

<sup>a</sup>Springel & Hernquist (2003, SH03)

<sup>b</sup>Faucher-Giguère et al. (2009, FG09)

NOTE—Model description of the Osaka20 simulation series. All simulations use a box size of comoving  $100 h^{-1}\text{Mpc}$  (cMpc), and  $2 \times 512^3$  particles for gas and dark matter. Further details of simulation parameters are given in Table 3 of Appendix B. See the main text for the details of baryonic spatial resolution. The first four runs adopt the Haardt & Madau (2012) UVB model. See Appendix B for the discussion of box-size effect and resolution test.

$5.38 \times 10^8 h^{-1}\text{M}_\odot$  for gas and dark matter particles. The gas particle mass can change due to star formation and feedback. The gravitational softening length is set to  $\epsilon_g = 7.8 h^{-1}\text{ckpc}$ , but we allow the baryonic smoothing length to become as small as  $0.1\epsilon_g$ . This means that the minimum baryonic smoothing at  $z = 2$  is about physical  $260 h^{-1}\text{pc}$ , which is sufficient to resolve the structures associated with Ly $\alpha$  forest. We adopt the following cosmological parameters from Planck Collaboration et al. (2016):  $(\Omega_m, \Omega_{\text{dm}}, \Omega_b, \sigma_8, h) = (0.3089, 0.2603, 0.04860, 0.8150, 0.6776)$ .

The list of simulations with different models are summarized in Table 1. Since the self-shielding of UVB might affect the Ly $\alpha$  forest via star formation and feedback (e.g., Rahmati et al. 2015), we perform two runs with and without self-shielding: ‘Osaka20-Shield’ and ‘Osaka20-Fiducial’, respectively. The third run (Osaka20-NoFB) in Table 1 is without SN feedback to test the impact of Osaka feedback model on the Ly $\alpha$  forest statistics. The fourth run (Osaka20-CW) is with the constant velocity galactic wind model by Springel & Hernquist (2003). The fifth run (Osaka20-FG09) uses the UVB model of FG09 instead of Haardt & Madau (2012) to examine the impact of slight differences in the UVB model.

## 2.2. Light-cone & Line-of-Sight (LoS) data set

Using the output of our cosmological SPH simulations, we first produce the light-cone data set for a redshift path of  $z \approx 2 - 3$  which is the primary redshift range

<sup>1</sup> <https://grackle.readthedocs.org/>

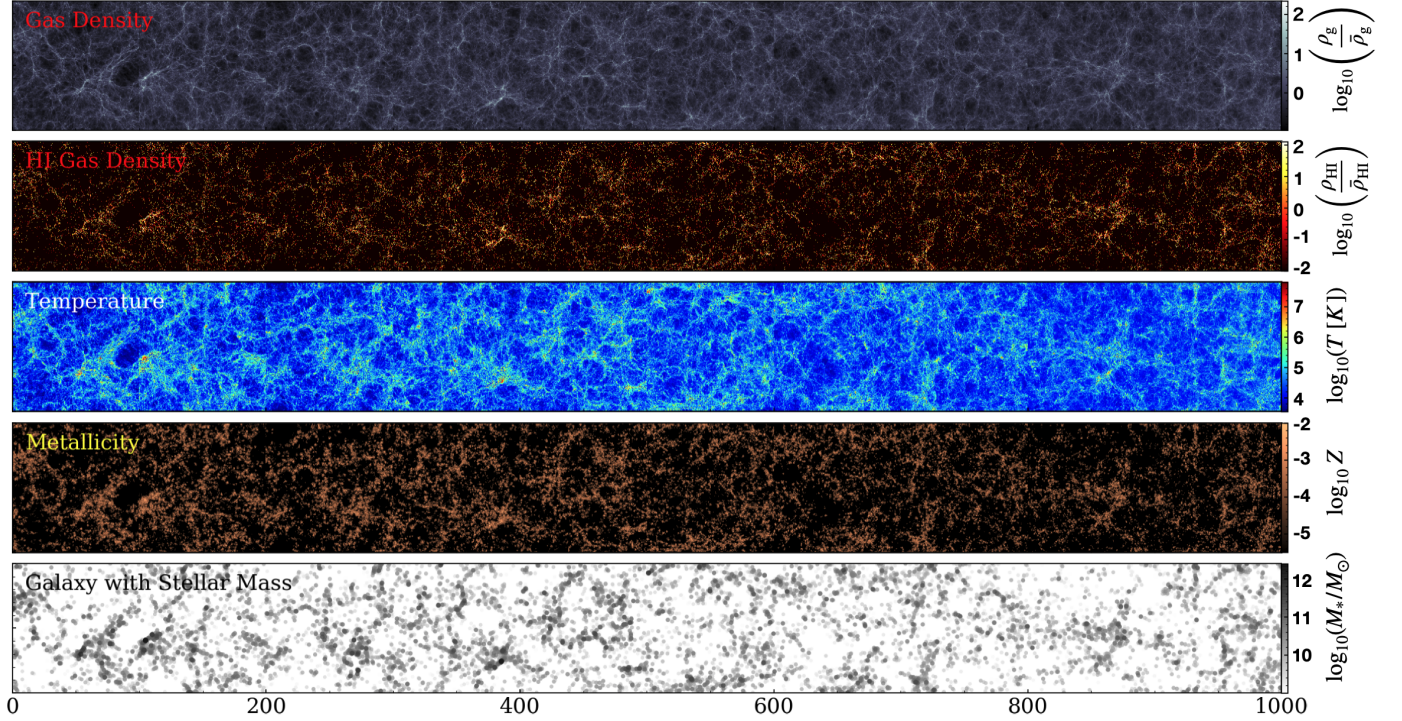


**Figure 1.** Light-cone output at  $z \approx 2 - 3$ , covering  $100 h^{-1} \text{cMpc}$  (height)  $\times 1 h^{-1} \text{cGpc} \times 10 h^{-1} \text{cMpc}$  (depth). From top to bottom panels: projected gas overdensity, HI overdensity, temperature, metallicity, and galaxy distribution color-coded by the stellar mass, respectively. In the bottom panel, one can see the galaxy bias effect where more massive galaxies are more clustered in high-density regions.

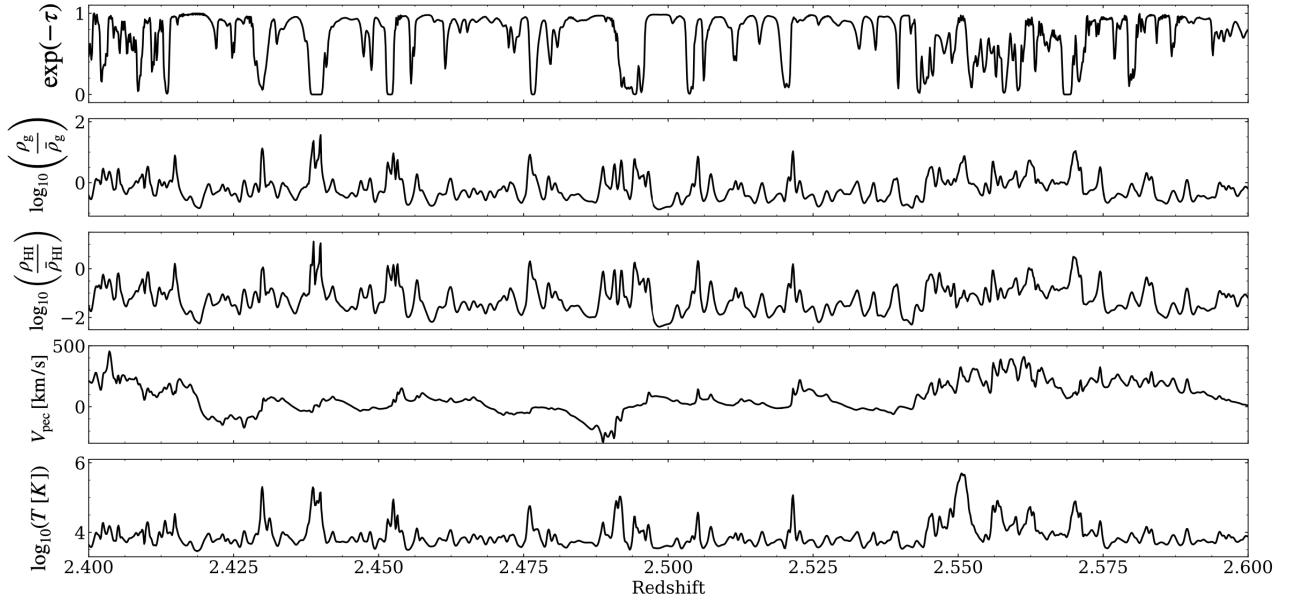


**Figure 2.** An example of line-of-sight data for  $z = 2.4 - 2.6$ . From top to bottom: transmitted flux (i.e.  $\exp(-\tau)$ ), total gas overdensity, HI overdensity, peculiar velocity along the LoS, and temperature distribution. One can see that the absorption trough is slightly shifted from the overdensity peaks due to peculiar velocities, and the HI overdensities sometimes do not match with the total gas overdensities in hot overdense regions (e.g. see the features associated with a high- $T$  peak at  $z \sim 2.55$ .)

of observed Ly $\alpha$  forest, as it conveniently falls into the optical wavelength range for ground-based spectroscopic observations. This is also the target redshift range for the IGM tomography by PFS (Takada et al. 2014). With JWST, we will be able to probe higher redshift range as well, but for the moment we focus on  $z = 2 - 3$  in the present paper. We create the light-cone data by connecting 10 simulation boxes of different redshifts following Shimizu et al. (2014), and cover from  $z \sim 1.8$  to 3.1. When connecting the simulation boxes, we randomly shift and rotate each box so that the same structures do not repeat on a single line-of-sight (LoS). This method causes discontinuities between the connected simulation boxes and it is a concern, however, we have checked that our statistical results such as the Ly $\alpha$  power spectrum do not change when we change the details of how we connect the boxes. In the future, we will compare the results with other methods such as the one used by Davé et al. (2010) and examine the impact on the Ly $\alpha$  forest more carefully. The resulting light-cone has transverse dimensions of  $100 h^{-1} \text{cMpc} \times 100 h^{-1} \text{cMpc}$  and  $1 h^{-1} \text{cGpc}$  sightline.

We then calculate the Ly $\alpha$  optical depth ( $\tau$ ) along the LoS. First, we calculate the physical quantities,  $A_{\text{pixel}}(x)$ , at each pixel  $x$  along LoS, such as HI density, LoS velocity and temperature as follows:

$$A_{\text{pixel}}(x) = \sum_j \frac{m_j}{\rho_j} A_j W(r, h_j), \quad (1)$$

where  $A_j$ ,  $m_j$ ,  $\rho_j$  and  $h_j$  are the physical quantity of concern, gas particle mass, gas density, and smoothing length of  $j$ -th particle, respectively.  $W$  is the SPH kernel function, and  $r$  is the distance between LoS pixel and gas particles. The pixel length ( $dl$ ) is set to a constant value of  $100 h^{-1} \text{ckpc}$ , which is higher resolution than any of the relevant Ly $\alpha$  observations. Then, we calculate the Ly $\alpha$  optical depth  $\tau(x)$  using these physical values at each pixel as

$$\tau(x) = \frac{\pi e^2}{m_e c} \sum_j f \phi(x - x_j) n_{\text{HI}}(x_j) dl, \quad (2)$$

where  $e$ ,  $m_e$ ,  $c$ ,  $f$ ,  $n_{\text{HI}}$ , and  $x_j$  are the electron charge, electron mass, speed of light, absorption oscillator strength, HI number density, and  $j$ -th pixel location, respectively.  $\phi$  is the Voigt profile, and we use the fitting formula of Tasitsiomi (2006) without direct integration. We draw 1024 ( $= 32^2$ ) LoS with regularly spaced intervals, resulting in mean transverse separation of  $3.3 h^{-1} \text{Mpc}$  which is comparable to the CLAMATO survey.

Figure 1 shows various physical quantities in the entire light-cone at  $z = 2 - 3$ , covering  $100 h^{-1} \text{cMpc}$  (vertical)

$\times 1 h^{-1} \text{cGpc}$  (horizontal path-length)  $\times 10 h^{-1} \text{cMpc}$  (depth). From top to bottom panels: total gas overdensity, HI overdensity, temperature, metallicity, and the galaxy distribution color-coded by galaxy stellar masses. One can see visually that the higher mass galaxies are more clustered in higher density regions as expected from their higher clustering strength. Since our simulation box is limited to  $100 h^{-1} \text{cMpc}$ , we do not have very massive galaxies with stellar masses  $M_* > 10^{12} M_\odot$  at  $z \sim 2$ . Ideally we would like to simulate larger volumes in the future, however, the box size of  $100 - 200 h^{-1} \text{cMpc}$  is currently the sweet spot due to the balance of numerical resolution, large-scale modes of power spectrum, and the computing power of current supercomputers.

Figure 2 shows an example of LoS data as a function of redshift at  $z = 2.4 - 2.6$ , giving more detailed view of absorption line profiles and density fluctuations. The four panels show, from top to bottom, the normalized transmitted flux (i.e.,  $\exp(-\tau)$ ), total gas overdensity, HI overdensity, baryon peculiar velocities, and temperature profiles. One can see that some absorption troughs are slightly shifted from the density peaks due to peculiar velocities. When the peculiar velocity is positive (negative), the absorption is redshifted (blueshifted).

Just to walk the reader through some numbers, in the flat Planck cosmology adopted in this paper, the redshift path of  $\Delta z \sim 0.1$  corresponds to a comoving distance of  $\Delta r \approx c \Delta z / H(z) \approx c \Delta z / (3.58 H_0) \approx 120 \text{cMpc}$  at  $z = 2.4$ , which roughly corresponds to one simulation box size. Therefore Fig. 2 is created by using about two simulation boxes of  $100 h^{-1} \text{cMpc}$  size.

### 3. RESULTS

#### 3.1. Ly $\alpha$ forest flux PDF

As a starting point of our analysis, we show in Fig. 3 the probability distribution function (PDF) of Ly $\alpha$  forest transmitted flux  $F = \langle e^{-\tau} \rangle$ . Here the higher value of  $F$  means more transmission, i.e., less absorption with lower  $\tau$ . Here, all flux PDFs are computed as histograms using all the LoS data in the relevant redshift range, which is a standard procedure.

Panel (a) shows the redshift evolution of flux PDF at  $\bar{z} = 2 - 3$  with 128 bins in between  $0 < F < 1$ . This is obviously higher resolution than the observational data points, but we also would like to examine the higher resolution PDF for the future. For example, the line for  $\bar{z} \sim 2$  covers the redshift range of  $z = 1.9 - 2.1$  in the light-cone data. As the effective optical depth  $\tau_{\text{eff}}(z) = -\ln \langle F(z) \rangle$  increases from  $z = 2$  to 3 (Becker et al. 2013), the absorption lines with high  $\tau$  increases, and the plateau at low- $F$  gradually rises. Here, we fol-

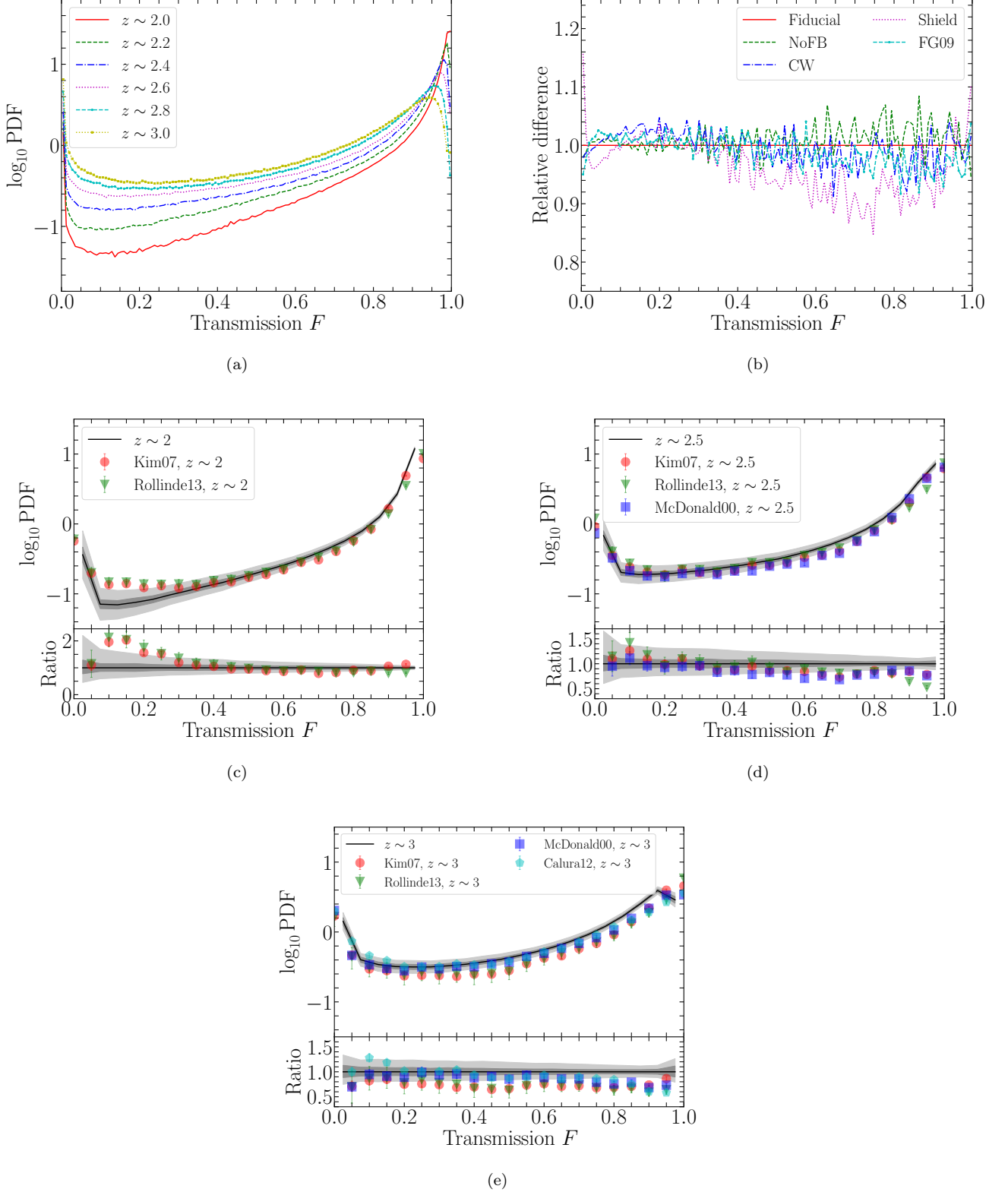


**Figure 3.** PDFs of Ly $\alpha$  forest transmission flux of all LOS from our fiducial run (Osaka20-Fiducial). *Panel (a)* shows the evolution of PDF from  $\bar{z} = 2 - 3$  for the Osaka20-Fiducial run. Here,  $\bar{z} \sim 2.0$  covers  $1.9 < z < 2.1$ ,  $\bar{z} \sim 2.2$  covers  $2.1 < z < 2.3$ , and so on. *Panel (b)* shows the difference of PDFs for five different runs relative to the Fiducial run at  $\bar{z} \sim 2.2$ . *Panels (c), (d), (e)* compare our results at  $\bar{z} \sim 2 - 3$  against the observational data of McDonald et al. (2000), Kim et al. (2007) and Rollinde et al. (2013). The black solid line is obtained by using the entire LoS dataset as in the observations. The shaded regions are  $1\sigma$  error estimated by jackknife method (dark grey) and  $1-\sigma$  variance of all LoS (light grey). The redshift coverage in panels (c), (d), (e) is the same as in Rollinde et al. (2013):  $\bar{z} \sim 2$  ( $1.88 < z < 2.37$ ),  $\bar{z} \sim 2.5$  ( $2.37 < z < 2.71$ ),  $\bar{z} \sim 3$  ( $2.71 < z < 3.21$ ). The bottom sub-panels of (c), (d), (e) indicate the offset between the black solid line and the observational data points.

low the standard practice of normalizing the simulated transmitted flux to  $\tau_{\text{eff}}(z)$  of [Becker et al. \(2013\)](#) in order to account for the uncertain UVB (e.g., [Viel et al. 2013b](#)). The peak at high  $F$  ( $> 0.9$ ) instead becomes less steep towards higher values of  $F$  as the redshift increases.

We also compare the results of different runs in [Fig. 3\(b\)](#) by showing the offset from the Fiducial run, again using the same 128 bins as in panel (a). We find that the overall shape of the PDF does not change very much, and the relative difference remains within  $\sim 5$  per cent for most of the runs. However, the scatter becomes larger at higher  $F$  values, and in particular for the ‘Shield’ run with 10 per cent deviation at  $F > 0.6$ . The Shield run has higher HI densities compared to the Fiducial run due to its self-shielding treatment, which explains the larger number of low  $F$  lines and hence less pixels at  $F > 0.6$ .

There have been somewhat mixed results over the years regarding the impact of feedback on flux PDF. For example, [Theuns et al. \(2002\)](#); [Kollmeier et al. \(2006\)](#); [Tepper-García et al. \(2013\)](#) suggested that the Ly $\alpha$  forest statistics is not largely affected by galactic wind because the hot supernova bubbles preferentially expand into the voids without affecting the filaments very much. [Kollmeier et al. \(2003\)](#) examined the impact of galaxy photoionization, and concluded that it has only a small impact on the conditional mean flux decrement of Ly $\alpha$  absorption. [Cen et al. \(2005\)](#) suggested that the volume filling factor of metal-enriched bubbles is a strong test for the strength of galactic wind feedback. Both [Viel et al. \(2013b\)](#) and [Chabanier et al. \(2020\)](#) argued that the AGN feedback can affect the flux PDF and 1-D power spectrum significantly. However, [Sorini et al. \(2020\)](#) showed that the impact of AGN feedback on the HI distribution around galaxies might not be so strong statistically speaking. Our simulations show that SN feedback can have moderate impact ( $\sim 5$  per cent) on the flux PDF.

In [Figs. 3\(c\),\(d\),\(e\)](#), we compare our result to the observational data points ([Kim et al. 2007](#); [Rollinde et al. 2013](#)) within the same redshift range as the observations. [Kim et al. \(2007\)](#) examined the flux PDF of 18 high-resolution quasar spectra observed with the Ultraviolet and Visual Echelle Spectrograph (UVES) on the Very Large Telescope (VLT) at  $\bar{z} = 2.07, 2.52$ , and  $2.94$  (from the LUQAS sample; [Kim et al. 2004](#)). In their analysis, they separated the metal absorption lines and focused only on the HI absorption. They found that the flux PDF is sensitive to the continuum fit in the range of  $0.8 < F < 1.0$  and to metal absorption at  $0.2 < F < 0.8$ , where  $F$  is the normalized flux. Kim et al.’s sample was

larger than that of [McDonald et al. \(2000\)](#), and their measurement was systematically lower by up to 30 per cent at  $0.2 < F < 0.8$ , which can be seen in our [Fig. 3e](#). They ascribed this discrepancy due to a combination of improved removal of metal lines and cosmic variance. [Rollinde et al. \(2013\)](#) analyzed four observational data sets: LP sample (18 UVES VLT spectra from [Bergeron et al. 2004](#)), the LUQAS sample, the [Calura et al. \(2012\)](#) sample, and the [McDonald et al. \(2000\)](#) sample. The sample covered the following redshift range:  $\bar{z} = 2$  ( $1.88 < z < 2.37$ ),  $\bar{z} = 2.5$  ( $2.37 < z < 2.71$ ),  $\bar{z} = 3$  ( $2.71 < z < 3.21$ ). They compared their result to the mock sample from the GIMIC hydrodynamical simulation ([Crain et al. 2009](#)), and found that the error estimated by the jackknife resampling method was smaller than the variance of the simulation result.

In [Figs. 3\(c\),\(d\),\(e\)](#), the black solid line shows the result from all LOS, the dark shade around it shows the  $1\sigma$  jackknife error obtained in a similar manner to the observations, and the wider light grey shade around it shows the  $1\sigma$  sample variance of all LOS. We estimated the jackknife error by dividing the 1024 LOS sample into 64 subsamples, and estimated the variance by excluding one subsample each time (i.e., 64 trials). The jackknife errors are of similar size to those of the observed data points, but the sample variance of the simulation data is somewhat larger, which is consistent with the results of [Rollinde et al. \(2013\)](#). We see rough agreement between the simulation and observations, but also some deviations depending on the range of  $F$  and redshift. For example, the simulation result is persistently higher than [Kim et al. \(2007\)](#)’s data by more than  $1\sigma$  at  $F > 0.3$  at  $\bar{z} \sim 3$ . The bottom sub-panels of [Figs. 3\(c\),\(d\),\(e\)](#) show the ratio between the black solid line and the observed data points. At  $\bar{z} \sim 2$ , the deviation becomes somewhat large at  $F < 0.3$ , but otherwise the simulation results and the data points agree with each other within 20 – 30 per cent. The discrepancy between observations and simulation result at the highest  $F$  values is nearly universal among hydrodynamic simulations of the Ly $\alpha$  forest, and in fact likely due to systematic continuum-fitting errors in the observational data ([Lee 2012](#)) rather than because of the simulations. [Bolton et al. \(2017\)](#) found that the observational data points were within  $2\sigma$  of the flux PDF from the SHERWOOD simulation, although in about half of the bins, the observational data were below the simulation result by more than  $1\sigma$ . They suggested that their simulation might be lacking hot underdense gas because adopting an isothermal temperature–density relation improves the agreement at  $0.1 < F < 0.8$ .

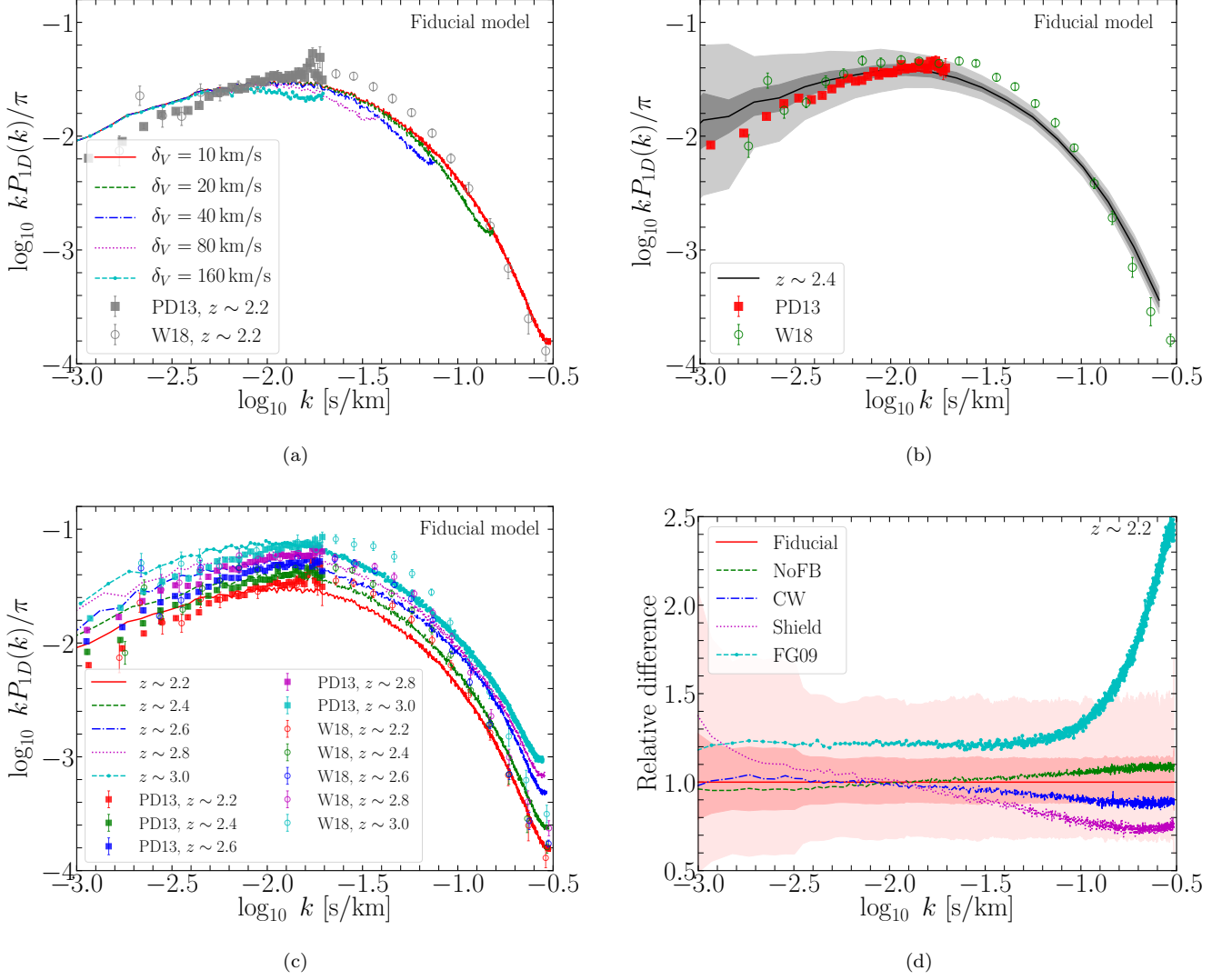


**Figure 4.** 1D power spectrum of Ly $\alpha$  forest as a function of velocity wave number. *Panel (a)* compares the  $P_{1D}(k)$  computed with different  $\delta_v$ -size for our Fiducial run at  $\bar{z} \sim 2.2$ . As the value of  $\delta_v$  becomes smaller, one can probe smaller scales more, and the upper end of  $P_{1D}(k)$  shifts to higher  $k$  with decreasing  $\delta_v$ . In all panels, the observational data points are from Palanque-DeLabrouille et al. (2013, P13) and Walther et al. (2018, W18). *Panel (b)* shows the  $P_{1D}(k)$  with  $1\sigma$  jackknife error (dark grey) and  $1\sigma$  variance of all LoS (light grey) in the Fiducial run using the same bins as W18 at  $\bar{z} \sim 2.4$ . *Panel (c)* shows the redshift evolution of  $P_{1D}(k)$  from  $\bar{z} = 2$  to 3 for the Fiducial model. *Panel (d)* compares  $P_{1D}(k)$  of different simulation models given in Table 1 relative to the Fiducial run. The pink shade is  $1\sigma$  (darker one) and  $3\sigma$  (thinner one) jackknife errors.

### 3.2. 1D Ly $\alpha$ power spectrum

In addition to the flux PDF, the one-dimensional (1D) power spectrum of Ly $\alpha$  forest  $P_{1D}(k)$  is another important observed statistic (Croft et al. 1998; McDonald et al. 2006; Palanque-DeLabrouille et al. 2013; Chabanier et al. 2019). In their pioneering work, Croft et al. (1998) presented a simple method to recover the shape and amplitude of the power spectrum of matter fluctuations from observations of Ly $\alpha$  forest using a fast Fourier transform (FT) method. Palanque-DeLabrouille et al. (2013) measured the  $P_{1D}(k)$  using 13821 high-

quality quasar spectra from SDSS-III/BOSS DR9 at  $z = 2.2 - 4.4$  on scales of  $k = 0.001 - 0.02 \text{ s km}^{-1}$ . They improved the constraints on cosmological parameters from SDSS by a factor of a few over the previous estimate by McDonald et al. (2006), deriving  $\sigma_8 = 0.83 \pm 0.03$  and  $n_s = 0.97 \pm 0.02$  assuming a flat- $\Lambda$  universe with no massive neutrinos, although without considering the astrophysical impacts of feedback in their hydrodynamic simulations. Viel et al. (2013b) examined the  $P_{1D}(k)$  using the OWLS cosmological hydrodynamic simulations (Schaye et al. 2010), and argued that the effect of galactic wind is comparable to the uncertainties of observed

power spectra, and must be taken into account for a robust and accurate measurement.

Here we follow Croft’s FT method for our calculation of  $P_{1D}(k)$  for its simplicity and clarity. Figure 4 presents  $P_{1D}(k)$  from our simulations compared with the observational data of Palanque-Delabrouille et al. (2013); Walther et al. (2018). Some previous numerical works have added a Gaussian noise of  $6 - 7 \text{ km s}^{-1}$  to the absorption profile data in order to mimic the observational error due to limited spectral resolution. Here, instead, we vary the velocity bin size when we compute the averaged absorption profile to evaluate the impact of spectral resolution. In Fig. 4(a), we show  $P_{1D}(k)$  for five different velocity bin-size of  $\delta_v = 10, 20, 40, 80,$  and  $160 \text{ km s}^{-1}$ . As expected, with smaller spectral bin sizes, the  $P_{1D}(k)$  reaches higher  $k$  and probe smaller scales. Note that  $\delta_v = 160 \text{ km s}^{-1}$  corresponds to  $\sim 2 h^{-1} \text{ cMpc}$  in the adopted cosmology. Our result with  $\delta_v = 10 \text{ km s}^{-1}$  captures the upper end of  $P_{1D}(k)$  very well at high- $k$ , but some differences can be seen at the intermediate scale of  $\log(k [\text{s/km}]) \sim -1.5$  and at the largest scales of  $\log(k [\text{s/km}]) \lesssim -2.5$ .

In Fig. 4(b), we compare our simulation results to the data of Palanque-Delabrouille et al. (2013); Walther et al. (2018) at  $\bar{z} \sim 2.4$  (using the light-cone data at  $z = 2.3 - 2.5$ ). In this panel, we compute the  $1\text{-}\sigma$  error (dark shade) by following the jackknife method (Kim et al. 2004; Lidz et al. 2006; Rollinde et al. 2013): i.e., divide the 1024 LOS sample into 64 sub-samples, computed the  $P_{1D}(k)$  from each subsample, and then estimated the  $1\sigma$  error given by the sub-samples within the same bins as W18 data points. Our jackknife errors are comparable to those on the W18 data points. Some of the deviations between simulation and the observed data points are within  $1\sigma$  error, but some are not. In the same panel, we also show the  $1\sigma$  variance of all 1024 LOS in light gray shade, which is larger than the  $1\sigma$  jackknife error.

Figure 4(c) shows the redshift evolution of  $P_{1D}(k)$  for the Fiducial run at  $z \sim 2.2 - 3.0$ . As the effective Ly $\alpha$  optical depth increases towards higher redshift, the normalization of  $P_{1D}(k)$  also rises, and our simulation captures this evolution qualitatively well, with similar levels of differences with observational data as in Fig. 4a,b. These differences with the observational data is understandable because we have not fine-tuned our IGM thermal state by tweaking the parameters of temperature–density relation ( $T \propto \rho^\gamma$ ) as other simulation works have done assuming the Fluctuating Gunn-Peterson Approximation (FGPA; e.g. Weinberg et al. 1998a; Croft et al. 1998; Sorini et al. 2016).

In Fig. 4(d), we compare simulations with different models listed in Table 1 against the Fiducial run at  $\bar{z} \sim 2.2$ . The same data points as in panel (a) are shown, as well as  $1\sigma$  and  $3\sigma$  jackknife errors in pink shade. We see that the FG09 run gives persistently higher power than the Fiducial run, which can be explained if FG09 run has more HI gas with less photoionization. In fact, this is consistent with the result by Rollinde et al. (2013) who derived a lower photoionization rate for FG09 UVB model (see their Fig. 9). The NoFB run has a stronger power at higher  $k$  range (but within  $1\sigma$ ), which can be explained by stronger clumping of HI in high-density regions due to lack of SN feedback. It is not very clear why the Shield run has more (less) power at lower (higher)  $k$  than the Fiducial run, and it deviates more than  $1\sigma$  at  $\log(k [\text{s/km}]) < -2.8$  and  $> -1.6$ .

### 3.3. Flux contrast vs. Impact Parameter

We define the Ly $\alpha$  “flux contrast”  $\eta_F$  as follows:

$$\eta_F = -\delta_F = 1 - \frac{F}{\langle F \rangle}, \quad (3)$$

where  $\delta_F$  is the absorption decrement integrated over a given velocity window within the 1D skewers, and  $F = \exp(-\tau)$  is the transmitted flux. The value of  $\eta_F$  increases to unity with stronger absorption due to greater amount of HI. In the opposite limit of smaller  $\tau$ ,  $\eta_F$  approaches zero when  $F$  approaches  $\langle F \rangle$ .

In Figure 5, we present  $\eta_F$  computed for various galaxy samples as a function of impact parameter  $b [h^{-1} \text{ cMpc}]$  from the galaxies (i.e., transverse distance). We first sit on a galaxy, take cylindrical bins around it with a fixed logarithmic bin size (dividing the range  $b = [10^{-2}, 50] h^{-1} \text{ cMpc}$  into 32 equal-sized logarithmic bins, count all LoS that come into the bin, and compute  $\eta_F$ . Each LOS can be associated with multiple galaxies. We use the full light-cone data and all galaxies within the volume, where the number of galaxies in each sample is  $N_{\text{gal}} = 3302, 48928, 195412, 277814$  for galaxy stellar mass limited samples of  $M_\star > 10^{11}, 10^{10}, 10^9, 10^8 M_\odot$ . We choose to divide the galaxy sample based on their stellar mass rather than the dark matter halo mass, because this way there is no ambiguity for substructures within massive halos. In the future, when the full Subaru PFS data set will become available, there will be a large galaxy catalogue with  $M_\star$  estimates, and we would be able to construct  $M_\star$ -limited samples of galaxies for these studies. We find a general trend that  $\eta_F$  increases with decreasing  $b$ , meaning that the amount of HI increases towards the center of galaxies. This trend is consistent with the earlier simulation results (e.g., Bruscoli et al. 2003; Kollmeier et al. 2003, 2006;

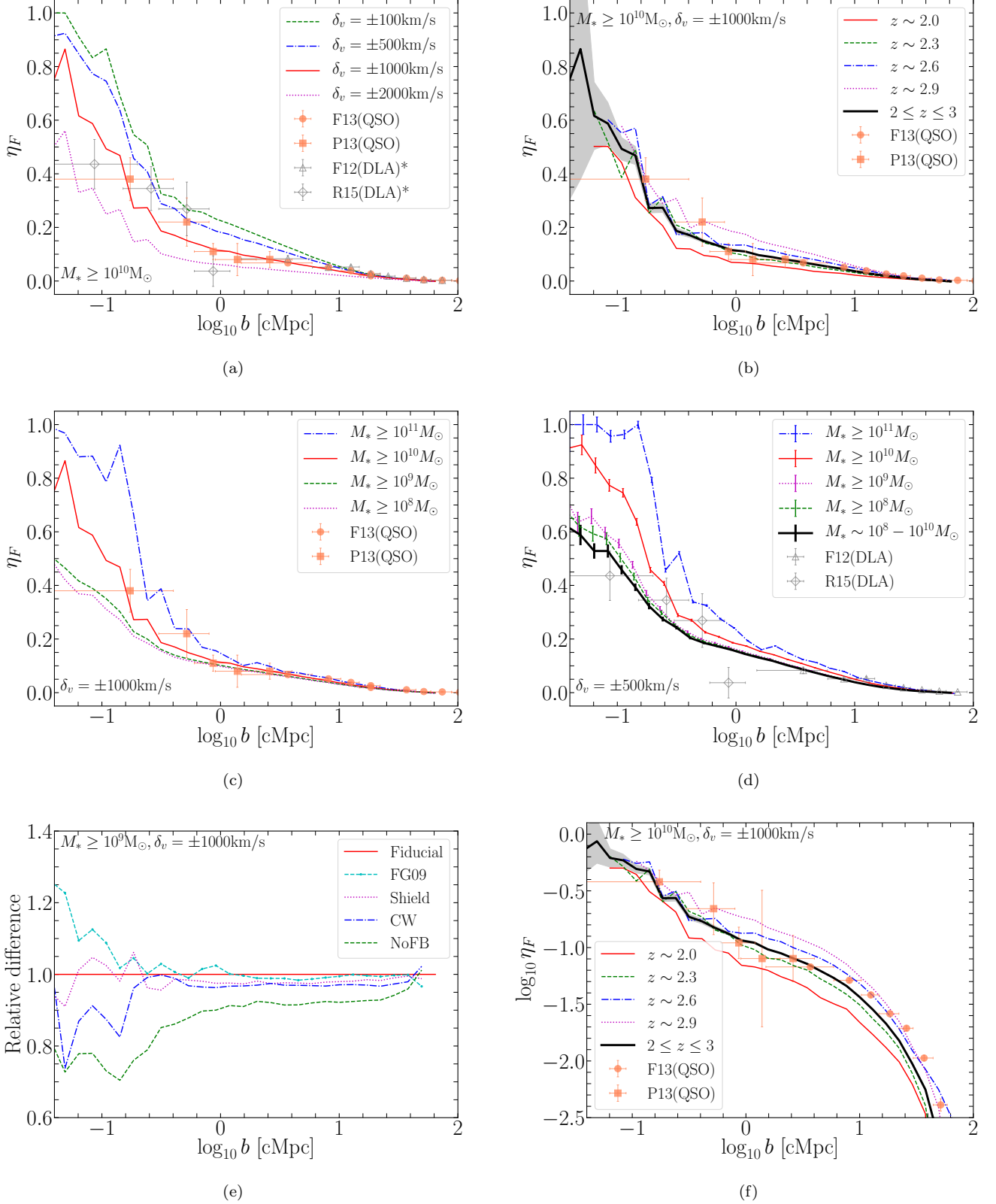


**Figure 5.** Flux contrast  $\eta_F$  vs. impact parameter  $b$  in units of comoving Mpc. Panel (a) compares the results computed with different search range  $\delta_v$ . Panel (b): Redshift evolution of  $\eta$  at  $\bar{z} = 2 - 3$ . The black solid line uses the entire light-cone data, and the grey shade represents the error  $\sigma/\sqrt{N}$ , where  $N$  is the data sample size in each bin. Panels (c), (d): Galaxy stellar mass dependency of  $\eta_F$ . Here the data points with error bars are taken from Sorini et al. (2018) who converted the cross-correlation signal from following authors to flux contrast: Font-Ribera et al. (2012, grey open triangle; F12), Font-Ribera et al. (2013, orange filled circle; F13), Prochaska et al. (2013, orange filled square; P13), and Rubin et al. (2015, grey open diamond; R15). The error bars in panel (d) represents  $\sigma/\sqrt{N}$ , where  $N$  is the data sample size in each bin. Panel (e): Comparison of different simulations listed in Table 1 relative to the Fiducial run for the full light cone. Panel (f): Logarithmic version of panel (b) to show the differences on large scales better. The grey shade on the black solid line is the same as in panel (b).

Meiksin et al. 2015; Turner et al. 2017; Meiksin et al. 2017; Sorini et al. 2018).

In Fig. 5(a), we compare  $\eta_F$  computed with different search ranges of  $\delta_v = \pm 500, \pm 1000, \& \pm 2000 \text{ km s}^{-1}$  along the LOS, and using the galaxy samples with stellar masses  $M_\star \geq 10^9 M_\odot$ . The value of  $\eta_F$  is expected to be higher (i.e., stronger absorption) for smaller  $\delta_v$  as it probes only the region closer to the galaxies. We compare our simulation results to the observational data points taken from Sorini et al. (2018), who converted the cross-correlation signal from following authors to the flux contrast: Font-Ribera et al. (2012, grey triangle; F12), Font-Ribera et al. (2013, orange circle; F13), Prochaska et al. (2013, orange square; P13), and Rubin et al. (2015, grey diamond; R15). The data of F13 and P13 are for  $\delta_v = \pm 1000$ , and F12 & R15 for  $\delta_v = \pm 500$  (hence with the asterisk in Fig. 5(a) to distinguish).

F12 measured the large-scale cross correlation between Ly $\alpha$  forest and damped Ly $\alpha$  systems (DLAs) using the 9th Data Release (DR9; Ahn et al. 2012) of the Baryon Oscillation Spectroscopic Survey (BOSS). They detected the cross-correlation signal on scales up to  $40 h^{-1} \text{ Mpc}$  which is fitted well by the linear theory prediction of CDM model with redshift distortions. The amplitude of the DLA–Ly $\alpha$  cross-correlation depends on the bias factor of DLA system as well as that of the Ly $\alpha$  forest.

Using a similar technique to F12, F13 also measured the cross-correlation between quasars and Ly $\alpha$  forest in the redshift space using 60,000 quasars spectra from the BOSS DR9. They found that the cross correlation can be fit well by the linear theory prediction at  $b > 15 h^{-1} \text{ cMpc}$ , and that the quasar bias to be  $3.64_{-0.15}^{+0.13}$  at  $\bar{z} = 2.38$ . They also argued that the failure of simple linear model at  $b < 15 h^{-1} \text{ Mpc}$  could be due to enhanced ionization by the quasar radiation, i.e., the quasar proximity effect (e.g., Bajtlik et al. 1988; Scott et al. 2000; Calverley et al. 2011).

Projected pairs of quasar (or QSO) sight-line allow us to study a foreground quasar’s environment in absorption lines. P13 used 650 quasar pair LOS to study the HI absorption transverse to luminous  $z \sim 2$  quasars at proper separations of  $30 \text{ kpc} < b < 1 \text{ Mpc}$ . Their analysis of composite spectra revealed excess Ly $\alpha$  absorption characterized by  $W = 2.3 \text{ \AA} (b/100 \text{ kpc})^{-0.46}$ . The excess of optically thick HI absorbers ( $N_{\text{HI}} > 10^{17.3} \text{ cm}^{-2}$ ) at  $b < 200 \text{ kpc}$  was described by a quasar-absorber cross-correlation function  $\xi_{\text{QA}} = (r/r_0)^\gamma$  with  $r_0 = 12.5_{-1.4}^{+2.7} h^{-1} \text{ cMpc}$  and  $\gamma = 1.68_{-0.30}^{0.14}$ , which is consistent with quasars being hosted by massive dark matter halos  $M_{\text{halo}} \sim 10^{12.5} M_\odot$  at  $z \sim 2.5$  according to P13.

Similarly to P13, R15 also used close pairs of quasars to probe the CGM transverse to 40 DLAs at  $1.6 < z_{\text{DLA}} < 3.6$ . From the analysis of average Ly $\alpha$  absorption profiles, they showed that the covering fraction of optically thick HI ( $N_{\text{HI}} > 10^{17.2} \text{ cm}^{-2}$ ) is  $\gtrsim 30\%$  within  $b < 200 \text{ kpc}$ , and that of SI II is  $20_{-8}^{+12}\%$  within  $b < 100 \text{ kpc}$ .

In Fig. 5(a), we see rough agreement with observational data for  $\delta_v = \pm 1000 \text{ km s}^{-1}$  within the error bars, and the agreement on large scales is particularly good as it converges to zero towards the edge of the simulation box. This convergence is natural because the mean transmission is rescaled to match  $\langle F \rangle$  as we explained in Section 3.1.

Figure 5(b) shows the redshift evolution of  $\eta_F$  as a function of impact parameter  $b$  for the Fiducial model. As the redshift becomes higher, the number of more massive galaxies decreases, and the signal on small scales becomes somewhat noisy at  $\log(b [\text{cMpc}]) \lesssim -1.0$ . Therefore we have truncated the lines at the smallest scale bins where we cannot make reliable measurements due to small statistics. In this panel we are using the galaxy sample with  $M_\star > 10^{10} M_\odot$  to compare with the data of F13 and P13 which are based on quasar sight-lines. Generally quasars are considered to reside in the most massive halos of  $M_{\text{halo}} > 10^{12} M_\odot$ , therefore taking the galaxy sample with  $M_\star > 10^{10} M_\odot$  would roughly correspond to such halos and be more appropriate. The logarithmic version of Fig. 5(b) is shown in Fig. 5(f), which shows the behavior of different models more clearly on large scales. A nice agreement within the error bars can be seen at  $\log(b [\text{cMpc}]) \lesssim 1.0$ . The data points are somewhat on the higher side at  $\log(b [\text{cMpc}]) \gtrsim 1.2$ , but since the ordinate is in log-scale, the actual deviation is small as seen in panels (a) and (b).

Figures 5(c),(d) shows  $\eta_F$  for different galaxy samples with stellar mass ranges of  $M_\star \geq 10^8, 10^9, 10^{10}, \& 10^{11} M_\odot$ . We find higher  $\eta_F$  values for more massive galaxies, as expected from higher bias of massive galaxies in more massive halos. Fig. 5(c) compares the simulation results to the data by F13 & P13 with  $\delta_v = \pm 1000 \text{ km s}^{-1}$ , and Fig. 5d to the data by F12 & R15 with  $\delta_v = \pm 500 \text{ km s}^{-1}$ . The lines for  $M_\star > 10^{10} M_\odot$  and  $> 10^{11} M_\odot$  in Fig. 5(c) shows a rough agreement with F13 & P13 data, and this is reasonable for the QSO sight-lines which would correspond to more massive halos with  $M_{\text{halo}} \gtrsim 10^{12} M_\odot$ . In Fig. 5(d) we see better agreement with lower  $M_\star$  samples with F12 & R15 data points based on DLAs, which is also reasonable because median DLA halos are expected to be somewhat lower mass halos with

$M_{\text{halo}} \lesssim 10^{12} M_{\odot}$  (e.g., Nagamine et al. 2007; Font-Ribera et al. 2012). Here the error bars on the simulation result are computed as  $\sigma/\sqrt{N}$  in each bin, where  $N$  is the number of LOS which came into the radial bin. In this panel we also show the line for the sample with  $10^8 < M_{\star} < 10^{10} M_{\odot}$  (thick black line), which is lower than those for  $M_{\star} > 10^{10} M_{\odot}$  or  $> 10^{11} M_{\odot}$ . This suggests that the  $\eta_F$  signal can be boosted strongly by the massive galaxies. In other words, the data points of F12 and R15 contain important contributions from lower mass galaxies with  $M_{\star} \leq 10^{10} M_{\odot}$  rather than just from a limited number of massive galaxies.

The dependence of  $\eta_F$  signal on the galaxy sample means that  $\eta_F$  may not be converged yet with the limited box sizes of our simulations (see also Appendix B). We caution the reader that the results of  $\eta_F$  could depend on the box size and associated galaxy mass range strongly, and our results may not have fully converged yet.

Figure 5(e) shows the results of  $\eta_F$  for different models and the simulation runs given in Table 1. This panel is computed with the galaxy sample of  $M_{\star} \geq 10^9 M_{\odot}$  and  $\delta_v \geq \pm 1000 \text{ km s}^{-1}$ . We find that the variation of  $\eta_F$  due to the model differences is less than 25 per cent, which is somewhat smaller than those due to  $\delta_v$  or  $M_{\star}$  dependence. All runs other than the NoFB run are consistent with the Fiducial run within 5 per cent at  $\log(b [\text{cMpc}]) \gtrsim -0.4$ . To further interpret the model dependencies, one should consider the impact of star formation. For example, one might naively expect that there will be more HI gas around galaxies for the NoFB run. However, it is known that galaxies become more dense and compact without galactic wind feedback (e.g., Yajima et al. 2017), and the dense gas in galaxies is vigorously converted into stars, which leads to the over-prediction of galaxy stellar masses. As a result of this compact HI distribution and over-consumption of HI gas into stars, the NoFB run has the lowest  $\eta_F$  near the galaxies among all models. In the CW run, the gas is ejected out of galactic potential more efficiently than other models with some overheating of IGM (Choi & Nagamine 2011), hence less amount of HI gas around galaxies compared to the Fiducial run. These results indicate that it is crucial to treat star formation and feedback in simulations to obtain accurate results of  $\eta_F$  at  $b \lesssim 1 \text{ cMpc}$ , and this statistic can be an important test of feedback models. The Shield run has a higher  $\eta_F$  than the Fiducial run up to 5% in a few bins on small scales, and these could be the dense cold ISM in the substructure galaxies near the central galaxy, which could be more prominent due to the self-shielding effect. The FG09 run also has a higher  $\eta_F$  than the Fiducial

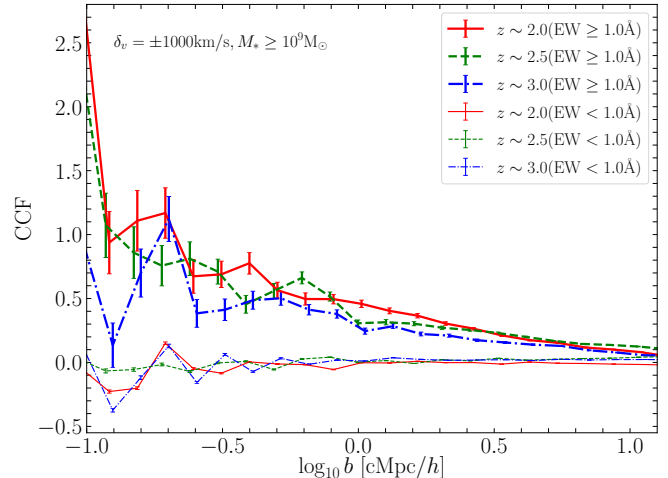


**Figure 6.** CCF between galaxies ( $M_{\star} \geq 10^9 M_{\odot}$ ) and HI absorbers with high EW ( $\text{EW} > 1 \text{ \AA}$ ; thick lines) and low EW ( $\text{EW} < 1$ ; thin lines) as a function of transverse distance between galaxies and LoS. High-EW systems have stronger correlations with galaxies, while low-EW systems are more broadly distributed, hence almost no correlation or negative correlation. See the main text for more details.

run by more than 10% at the smallest scales of  $b \lesssim 10 \text{ kpc}$ , which can be ascribed to lower photoionization rates than in the HM12 model (see also Sec. 3.2 and Fig. 4d).

#### 3.4. Cross-correlation between galaxies and HI

We use the same LOS and galaxy samples to compute the cross-correlation function (CCF) in the following. We first sit on a galaxy, take cylindrical bins around it with equal logarithmic bins (32 logarithmic bins for the range of  $b = [0.01, 20] h^{-1} \text{ cMpc}$ ), count all LOS that come into the bin, and compute CCF between the galaxy and the pixels along the LOS. Each LOS can be associated with multiple galaxies.

Figure 6 shows the CCF between the simulated galaxies with  $M_{\star} \geq 10^9 M_{\odot}$  and discrete HI absorbers with high equivalent width (EW) ( $\text{EW} > 1 \text{ \AA}$ ; thick lines) and low EW ( $\text{EW} < 1$ ; thin lines) as a function of transverse distance between galaxies and LoS. As for the CCF, we use a simple estimator of  $(DD/DR) - 1$ , where  $DD$  and  $DR$  are the number of pairs found in data–data and data–random data sets. Here the EW is simply measured as a boxcar EW. For a more accurate treatment, it requires a photo-ionization calculation using a code like Cloudy, and measure the HI column density via Voigt profile fitting. We plan to present such analyses together with metal absorption lines in the future. Here, for a simple examination of dependence of CCF on the HI column density, we divide the sample into two samples of high- and low-EW systems, and compute the

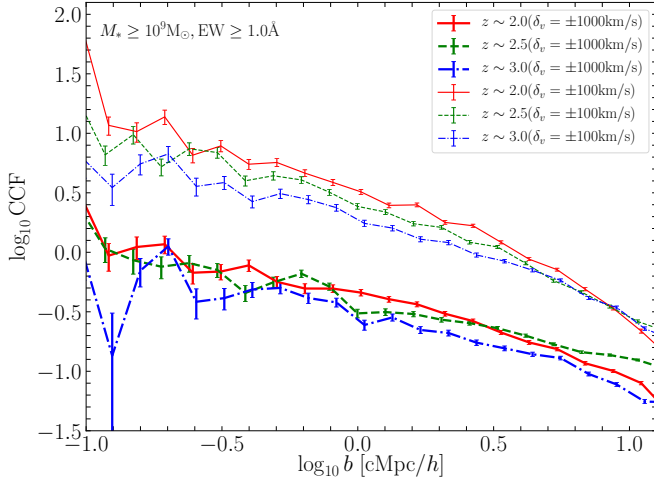


**Figure 7.** Dependence of CCF on the search range along LoS. The thick lines are for search path-length of  $\delta_v = \pm 1000 \text{ km s}^{-1}$ , and thin lines are for  $\delta_v = \pm 100 \text{ km s}^{-1}$ . The latter case is only looking at correlations between close pairs of absorbers and galaxies, hence producing stronger CCF signal. For all cases, galaxies with  $M_* > 10^9 M_\odot$  and HI absorbers with high-EW ( $\text{EW} > 1 \text{ \AA}$ ) were used.

CCFs separately at each redshift. In other words, our analysis presented here is performed with unsmoothed, finely sampled HI absorption lines compared to the actual observations.

The high-EW systems have stronger correlations with galaxies as expected, while the low-EW systems are more broadly distributed in space, hence almost no correlation (or even slightly negative correlation on small scales) relative to the galaxies. Note that the ordinate is in a linear scale in this plot to show the negative correlation at the same time. A weak redshift evolution is visible in Fig. 6, with stronger correlations at  $z = 2$  than at  $z = 3$  due to the evolution in  $\tau_{\text{eff}}$  (Becker et al. 2013). The Poisson error bars are computed as  $(1 + \text{CCF})/\sqrt{D_{\text{gal}}D_{\text{abs}}}$ , where  $D_{\text{gal}}$  and  $D_{\text{abs}}$  are the number of galaxy pairs and absorber pairs in each bin, respectively.

When computing the pairs for the CCF, it is not so obvious how deeply one should search for those pairs along the LoS. In order to examine the impact of search range  $\delta_v$ , we repeat the CCF calculation with two different values of  $\delta_v = \pm 1000$  &  $\pm 100 \text{ km s}^{-1}$ , and show the results in Fig. 7. We first sit on a galaxy, and search for the HI absorbers within  $\pm \delta_v$  from the systemic velocity of the galaxy along the LoS. The thick and thin lines are with  $\delta_v = \pm 1000 \text{ km s}^{-1}$  and  $\pm 100 \text{ km s}^{-1}$ , respectively. The latter case is only looking at the correlations between close pairs of absorbers and galaxies, hence pro-

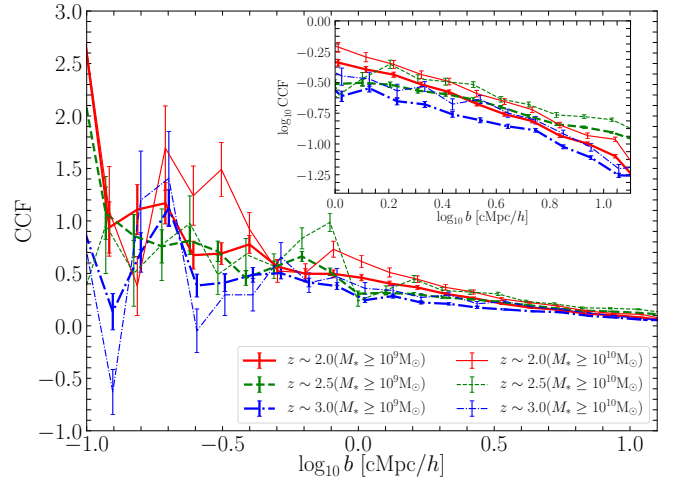


**Figure 8.** Dependence of CCF on the stellar mass of galaxies of concern. The thick lines are for galaxies with  $M_* > 10^9 M_\odot$ , and thin lines are for those with  $M_* > 10^{10} M_\odot$ . For all cases, HI absorbers with high-EW ( $\text{EW} > 1 \text{ \AA}$ ) and the search range of  $\delta_v = \pm 1000 \text{ km s}^{-1}$  were used.

ducing stronger CCF signals. For all cases, galaxies with  $M_* > 10^9 M_\odot$  and high-EW absorber sample were used.

In Figure 8, we show the dependence of CCF signal on galaxy stellar mass. The number of galaxies with  $M_* > 10^{10} M_\odot$  becomes smaller at  $z = 3$  in our simulation, and the number of CCF pairs also becomes less, resulting in the somewhat noisy CCF signal on small scales. (For example, there are 3515 galaxies between  $2.9 < z < 3.1$ , which corresponds to two simulation snapshots of  $100 \text{ cMpc/h}$  box.) At least, we see that the overall CCF signal is stronger for the  $M_* > 10^{10} M_\odot$  sample (thin lines) than for the  $M_* > 10^9 M_\odot$  sample (thick lines). This is consistent with the stellar-mass trend which we saw in Fig. 5(c),(d).

Figure 9 shows the 2D CCF between galaxies and HI with contours showing 16 levels between min/max in logarithmic scale. Consistently with the previous observational and simulation results (Rakic et al. 2012, 2013; Turner et al. 2014, 2017), we find the finger-of-god signature of elongation along the LoS direction with a stronger CCF signal. We intend to carry out further analysis of gas dynamics (inflow/outflow) to figure out what's really causing this finger-of-god signature. To detect this effect, Fig. 9 shows that it requires a transverse resolution of  $< 1 \text{ cMpc/h}$ . For example, Turner et al. (2017) compared the results of Keck Baryonic Structure Survey (KBSS) and the EAGLE cosmological simulations, and found good agreement in the 2D enhancement of HI optical depth near galaxies out to  $2 \text{ pMpc}$ , as well as detecting the finger-of-god-like feature. From the examination of median ion mass-weighted radial velocities,

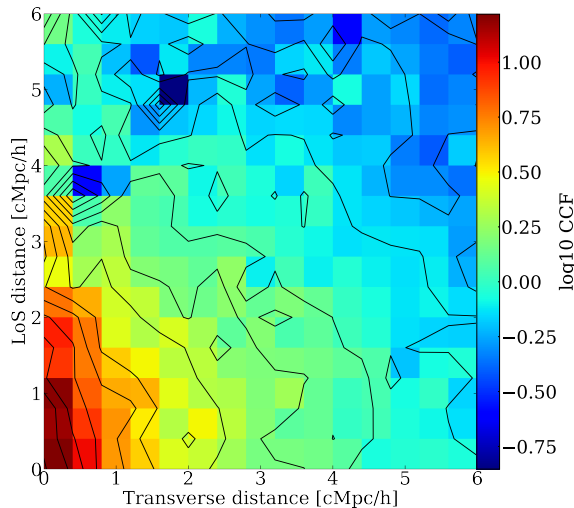


**Figure 9.** Two-dimensional CCF between galaxies and HI with contours showing 16 levels between the min/max values ( $-0.85/1.22$ ) in logarithmic scales.

they concluded that the feature was caused predominantly by the infalling gas motion rather than redshift errors.

### 3.5. Comparison with the ‘Mukae plot’

Even if one does not have spectroscopic data, photometric data of galaxies are also useful to investigate macroscopic relations between gas and galaxies. The combination of spectroscopic and imaging surveys are powerful if we could perform IGM tomography. For example, Fig. 8 of Mukae et al. (2020) compares the LAE overdensity filaments with gas filaments from the IGM tomography.

Using the photometric galaxy catalog from the COSMOS/UltraVISTA (Muzzin et al. 2013), Mukae et al. (2017) detected a weak correlation between galaxy overdensity ( $\delta_{\text{gal}}$ ) and Ly $\alpha$  absorption decrement ( $\delta_F$ ) in cylinders with a base radius of  $r = 5'$  ( $\sim 2.5$  pMpc at  $z \sim 2.5$ ) and a cylinder length of 25 pMpc which corresponds to their photometric redshift uncertainty. Their galaxies lie at  $2 < z < 3$ , and stellar masses were estimated by the SED fitting using the FAST code (Kriek et al. 2009). They applied a criteria of  $K < 23.4$  mag which corresponds to a stellar mass limit of  $\log(M_*/M_\odot) > 9.7$  at  $z \sim 2.5$ . In the following, we call this correlation plot between  $\delta_{\text{gal}}$  and  $\delta_F$  a ‘Mukae plot’. They found a weak negative correlation of

$$\delta_F = \alpha \delta_{\text{gal}} + \beta \quad (4)$$

with  $\alpha = -0.14^{+0.06}_{-0.16}$  and  $\beta = -0.17^{+0.06}_{-0.06}$ .

In Fig. 10a, we show the result from our light-cone data (with the total galaxy sample of  $M_* > 10^{9.7} M_\odot$ ) estimated with the same cylinder size and  $M_*$ -limit as Mukae et al. (2017) at  $z = 2 - 3$ . The smaller red dots represent our measurements in each cylinder in our light-cone data, which show a greater scatter than Mukae’s result. The bigger red points with error bars are the average of smaller red dots, covering the entire distribution with eight equal-sized bins. The red solid line is the least-square fit to the median points with  $1-\sigma$  error bars with  $\alpha = -0.066 \pm 0.0011$  and  $\beta = -0.100 \pm 0.00060$ . Our simulation result has a shallower slope than the Mukae’s fit. The number of data points by Mukae et al. (2017) is much smaller than our simulated data points, and their fit may have been affected strongly by the outliers with low  $\delta_{(F)}$  values ( $\sim -0.4$ ).

In Fig. 10b, we compare our simulation result against the observational data by Liang et al. (2021), who made similar measurements of  $\delta_{\text{gal}}$  (with 2642 Ly $\alpha$  emitters at  $z \sim 2.2$ ) using a cylinder with a base aperture radius of 10 cMpc and a length of 62.5 cMpc (the FWHM of the NB387 filter) along the LoS. As for  $\delta_F$ , the averaging along the LOS was done over  $10 h^{-1}$  cMpc, i.e., 21.4 cMpc assuming  $h = 0.7$ , and the center of an absorber was searched as the absorption peak around  $3,862 \pm 35 \text{ \AA}$  ( $z \approx 2.15 - 2.20$ ). They also found a positive correlation between LAE overdensity and the effective Ly $\alpha$  optical depth estimated from 64 eBOSS quasar spectra. Liang et al. (2021) gave the best-fit results of  $\alpha = -0.116^{+0.018}_{-0.022}$  and  $\beta = -0.248^{+0.082}_{-0.093}$  (for all four fields) and  $\alpha = -0.227^{+0.026}_{-0.023}$  and  $\beta = -0.258^{+0.096}_{-0.114}$  (without the J0210 field).

Correspondingly, we made similar measurements using the total galaxy sample of  $M_* > 10^9 M_\odot$  in our light-cone data with the same cylinder size and LOS path-length, while the only difference of placing our cylinders at the redshift of concern, covering  $\pm L/2$  where  $L = 21.4$  cMpc. Our best-fit result gives  $\alpha = -0.0664 \pm 0.00476$  and  $\beta = -0.0938 \pm 0.00238$ , which is close to Liang’s result. The number of data points of Liang et al. is much larger with more scatter than those of Mukae’s, which could be one of the reasons for the shallower slope. See their §5.1 for further discussions on the sample bias. It is nevertheless interesting that a similar galaxy–HI correlation is obtained even in an extreme system such as the MAMMOTH region (Cai et al. 2016; Liang et al. 2021) to that of Mukae’s more general field. The exact value of intercept parameter  $\beta$  is probably not so important at this point, as each observational result is based on a different sample of galaxies with different normalization.

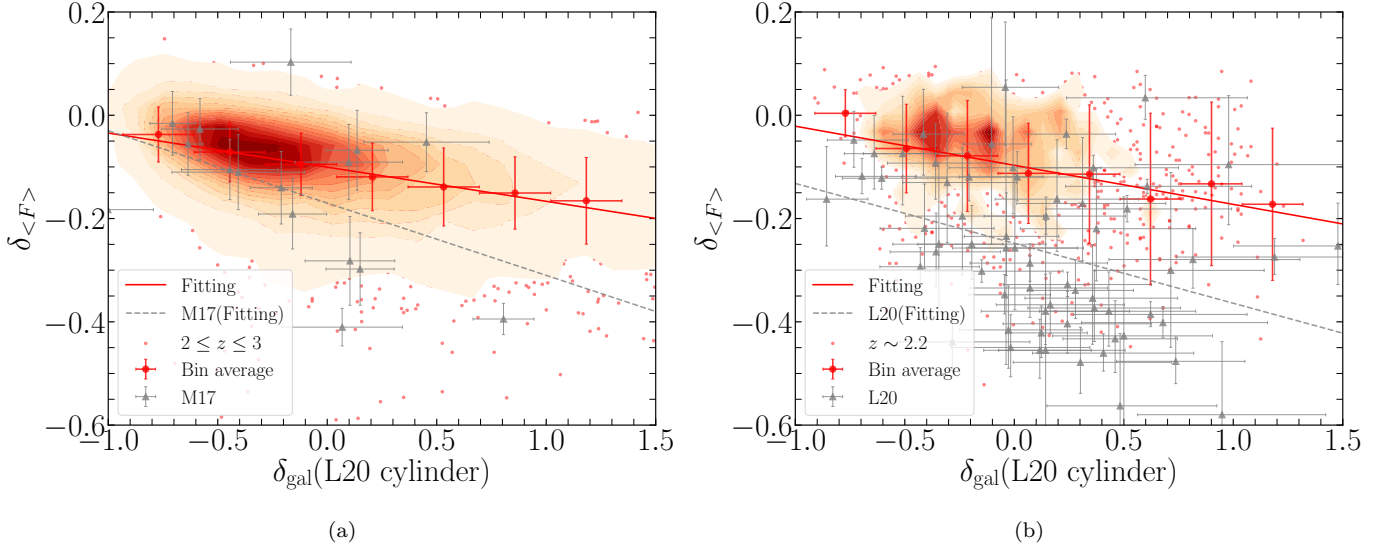


**Figure 10.** Relation between the flux contrast  $\delta_F$  vs. galaxy overdensity  $\delta_{\text{gal}}$ , compared against observational data. *Panel (a)* compares the simulation result against the observational data of Mukae et al. (2017, grey data points and their linear regression fit shown by the grey line). Each small red dot corresponds to one cylinder along the LOS in our simulation, with their mean in each  $\delta_{\text{gal}}$ -bin (covering the entire distribution with eight equal-sized bins in abscissa) and the linear regression fit to all the data points is shown in red solid line. *Panel (b)* compares against Liang et al. (2021)’s observational data. Here,  $\delta_F$  is computed within a length of  $15 h^{-1} \text{cMpc}$ , i.e.,  $21.4 \text{cMpc}$  assuming  $h = 0.7$  along the LOS, and  $\delta_{\text{gal}}$  is computed using a cylinder with an aperture radius ( $10 \text{cMpc}$ )  $\times 62.5 \text{cMpc}$  (length along the LoS  $\approx$  FWHM of NB387 filter). Note that the path-length to compute  $\delta_F$  and the cylinder size for  $\delta_{\text{gal}}$  are different between panels (a) & (b). We use the red contour to avoid saturation of points, which is constructed with  $32 \times 32$  grid with 16 equal logarithmic levels between minimum (4 dots) and maximum surface density of red dots.

Liang et al. (2021) also presented the results from our simulation using different galaxy samples of  $M_\star = 10^8 - 10^9, 10^8 - 10^9$ , and  $10^9 - 10^{10} M_\odot$ , and showed that the slope ‘ $\alpha$ ’ became shallower only by  $\Delta\alpha \sim 0.3$  for more massive galaxy sample. This trend is consistent with the naive expectation that the more massive galaxies are associated with deeper potential wells and more abundant HI gas in them. It is also consistent with our earlier results shown in Fig. 5(c),(d), where a stronger flux contrast is detected around more massive galaxies.

Given that the dependence of the slope on galaxy stellar mass is weak in our simulation, Liang et al. (2021) proposed that the attenuation of Ly $\alpha$  emission by the intergalactic HI might be the more dominant effect in lowering  $\delta_{\text{LAE}}$  (and hence making the slope ‘ $\alpha$ ’ steeper) rather than the different galaxy stellar mass of the sample. The spatial offset of LAEs from general galaxies are also observed statistically by Momose et al. (2021) and Momose et al. (2021b, accepted). Mukae et al. (2020) also pointed out the photoionization effect by the radiation from galaxies and quasars, producing proximity zones (e.g., Bajtlik et al. 1988; Scott et al. 2000; Calverley et al. 2011). To verify these arguments, we would have to perform Ly $\alpha$  radiation transfer calcula-

tions through IGM, which we plan to carry out in the future.

### 3.6. Flux contrast around a proto-cluster

Proto-clusters have been one of the interesting focus of high- $z$  galaxy studies. Given that they are biased regions with early evolution of density field, they can give us important insight in the early structure formation and help us to check the  $\Lambda$ CDM model during the critical phase of structure formation, when it is strongly driven by gravitational instability. Using protoclusters as cosmological probes can also highlight the importance of environmental effect of cosmic star formation rate density (e.g., Chiang et al. 2017), and the filamentary distribution of cosmic gas (e.g., Umehata et al. 2019).

The definition of a protocluster may vary depending on authors, but usually it is either a high concentration of galaxies at high redshift (e.g., Toshikawa et al. 2016; Toshikawa et al. 2017), or specifically meaning progenitors of present-day galaxy clusters in numerical simulations. In the actual observations, one cannot follow the time evolution of a system at a certain redshift to the present day, so one has to rely on other theoretical arguments, e.g., estimate the dark matter halo mass and

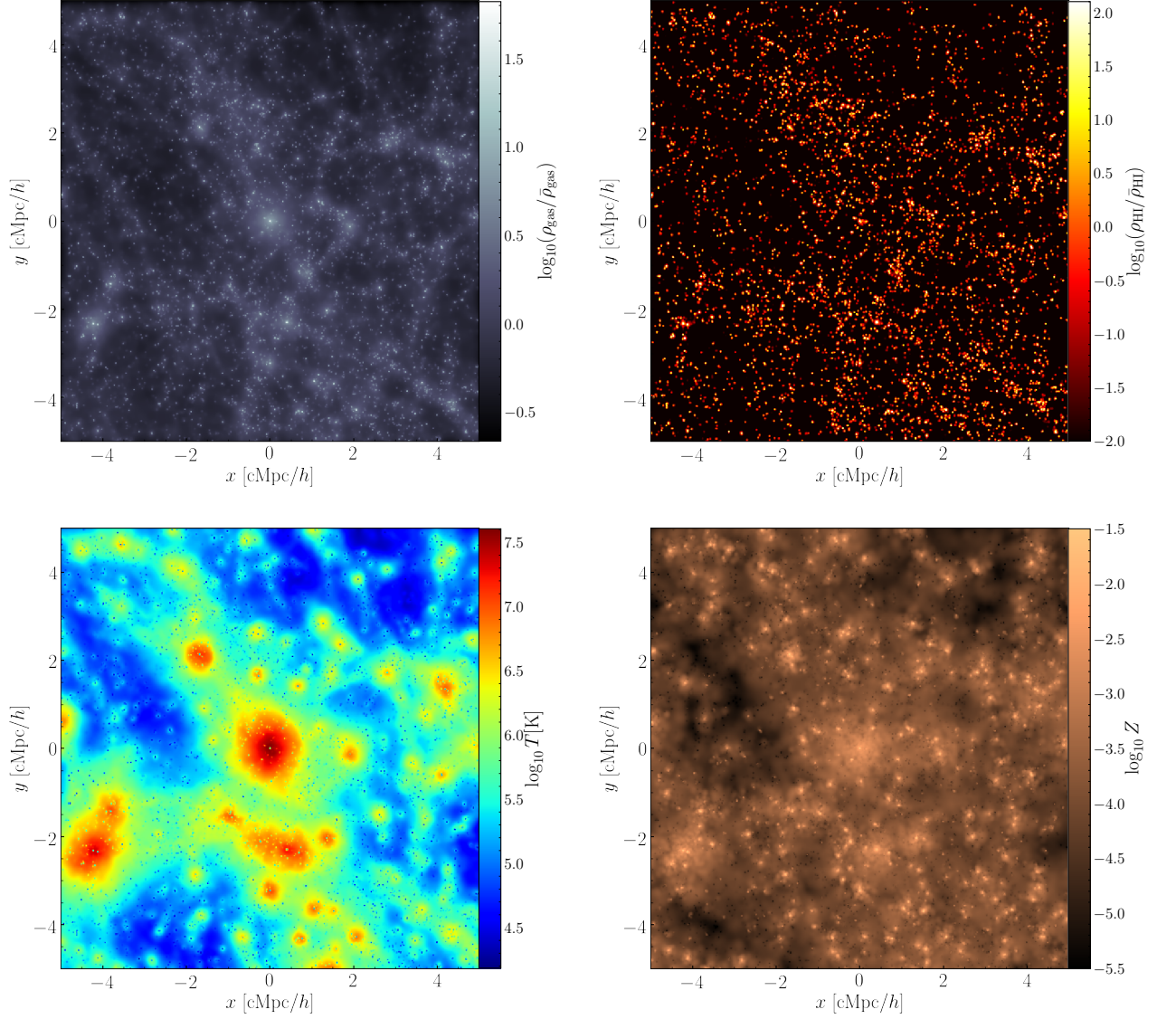


**Figure 11.** Projected maps of various quantities (gas overdensity, HI overdensity, temperature, metallicity, from top-left to bottom-right, respectively) in the proto-cluster region, which is the most massive system in our light-cone data. The mass of the proto-cluster is  $M_h = 9.4 \times 10^{13} h^{-1} M_\odot$  at  $z \sim 2.1$ , and the virial radius is  $R_v = 1.1$  cMpc.

refer to the results of  $N$ -body simulation for statistical connection between high- $z$  and low- $z$  sample.

Future IGM tomography studies will be able to identify numerous protoclusters without relying on spectroscopic follow-up of galaxies. In fact, Lee et al. (2016) discovered an extended IGM overdensity with deep absorption troughs at  $z = 2.45$  associated with a pre-discovered protocluster at the same redshift. They estimated that this IGM overdensity is associated with dark matter mass of  $M_{\text{DM}}(z = 2.45) \sim 1.1 \times 10^{14} h^{-1} M_{\odot}$ , which will later grow into a galaxy cluster with  $M_{\text{DM}}(z = 0) \sim 3 \times 10^{14} h^{-1} M_{\odot}$ . Krolewski et al. (2018) also reported a discovery of a cosmic void at  $z \sim 2.3$  using 3D Ly $\alpha$  tomographic map. Therefore it would be desirable to study tomographic properties of protoclusters in cosmological hydrodynamic simulations with full physics, and see if we find similar physical properties.

Figure 11 shows the projected quantities around a proto-cluster at  $z \sim 2.1$  with a halo mass of  $M_{\text{h}} = 9.4 \times 10^{13} h^{-1} M_{\odot}$  and a virial radius of  $R_{\text{v}} = 1.1$  cMpc. This is the most massive system in our light-cone data set. There is a clear high-overdensity region in the center of upper left panel of gas density field. Correspondingly the high-temperature ( $T \gtrsim 10^7$  K) intra-cluster gas is also visible in the center of the lower left panel, which would emit X-rays. The central region of this proto-cluster is already enriched to  $\log(Z/Z_{\odot}) \sim -1.5$  by  $z = 2.1$ . On the other hand, it is interesting to see that the protocluster is not so visible in the HI overdensity map in the upper right panel, because the HI gas is more localized in the centers of galaxies and not as prominent as the hot X-ray emitting intra-cluster gas within the proto-cluster.

Figure 12 shows the flux contrast as a function of transverse distance from the center of the proto-cluster at  $z \sim 2.1$  in cyan crosses, which covers the range of  $b = [0.02, 64]$  cMpc with eight equal-sized logarithmic bins. Note that the observational data points are shown only for comparison purposes, and we caution that each data set probes different median redshift from the proto-cluster. On large scales of  $b > 1$  cMpc, the flux contrast signal converges to the large-scale IGM signal, but we see an enhancement of signal at  $b < 200$  ckpc towards the center of the proto-cluster, even though it's not really visible to our eyes in the upper right panel of Fig. 11. In particular, in the inner-most bin of  $b \simeq 100$  ckpc, we see an enhancement by a factor of  $\sim 2$  over the observed data points. The proto-cluster flux contrast is inbetween those for the galaxy population of  $M_{\star} \geq 10^{10}$  and  $M_{\star} \geq 10^{11} M_{\odot}$ . This is reasonable, as we are approaching to the proto-cluster center where the brightest cD galaxy may be developing in the core. Our result is

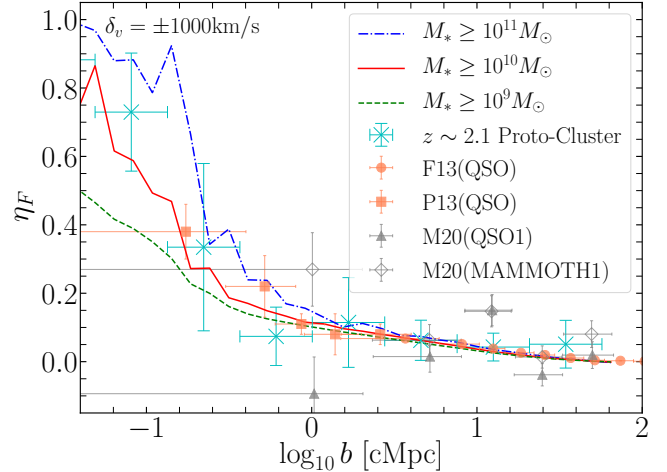


**Figure 12.** Flux contrast around the proto-cluster shown in Fig. 11 at  $z \sim 2.1$  as a function of transverse distance from the protocluster center. The cyan crosses show the average flux contrast in each transverse bin, and each data point is an average of eight LoS with the error bar showing the min/max scatter. The other observational data points and lines are the same as in Fig. 5d and shown for comparison. Additionally, black open circles are from Mukae et al. (2020), possibly indicating quasar proximity effect.

also in line with that of Miller et al. (2019), in the sense that the high- $\tau$  sightlines are dominated by galaxies and DLAs, whereas most of the sightlines simply have lower  $\tau$ . When the contribution from proto-cluster galaxies are averaged over in spherical shells, it can produce the increasing flux contrast towards the proto-cluster center.

In Fig. 12, we are also showing the data points from Mukae et al. (2020), who studied the 3D distribution of HI around quasars in the MAMMOTH-1 nebula (Cai et al. 2017) at  $z = 2.3$  using HI tomography technique. Their 3D radial HI radial profile showed a weaker absorption near the MAMMOTH-1 QSO, suggesting a proximity zone of photoionized gas (e.g., Bajtlik et al. 1988; Scott et al. 2000; Calverley et al. 2011). Here, for a fair comparison with our simulation results, we show the R2D estimate taken from their Fig. A1 in Appendix for MAMMOTH1-QSO and QSO1. The MAMMOTH1-QSO result is closer to the P13 data, but the QSO1 data shows a stronger decline in  $\eta_F$  on small scales of  $\log(b[\text{cMpc}]) \simeq 0.0$ .

We also note that Momose et al. (2021) detected weaker HI absorption within central few cMpc around AGNs, and that the maximum absorption is at  $r = 5 - 6 h^{-1}$  cMpc, again suggesting proximity effect. The differences between the data points by Prochaska et al. (2013) and Mukae et al. (2020)'s QSO1 data can be reconciled with anisotropic emission from quasars (see § 6.3 of Prochaska et al. (2013) for further discussions).

Therefore, if we want to study 3D distribution of HI around quasars and AGNs, a realistic model of AGN feedback is desired in simulations. On the other hand, Sorini et al. (2020) showed that, on average, the impact of AGN is not so strong compared to stellar feedback on Ly $\alpha$  forest statistics. It is clear that more detailed studies are needed to figure out when and how AGN feedback affects Ly $\alpha$  forest statistics, and we plan to do so in the future.

#### 4. DISCUSSION & SUMMARY

In preparation for the upcoming Subaru PFS survey and other major telescopes such as TMT and JWST, we produce the light-cone and LoS data sets at  $z = 2 - 3$  using the GADGET3-OSAKA cosmological hydrodynamic simulations with star formation and SN feedback models. We compute various Ly $\alpha$  forest statistics including 1D flux PDF, 1D power spectrum, cross-correlation function, and flux contrast as a function of transverse distance from galaxy centers and a proto-cluster.

We draw 1024 LoS to compute the Ly $\alpha$  forest data, and find that the 1D flux PDF shows a rough agreement with observations, although with some deviations depending on the value of  $F$  and redshift. Our jackknife estimate of  $1\sigma$  error is comparable to that of the observational estimates, but the sample variance is larger than the jackknife estimate, consistently with previous work (Kim et al. 2004; Rollinde et al. 2013). We checked that the variance does not change very much even if we draw 16384 LoS, which means that our results do not change very much by increasing the number of LoS further. The redshift evolution of the flux PDF is as expected, where the fraction of low-transmission lines increases with increasing  $\tau_{\text{eff}}$  towards higher redshift. We find that the different models of SN feedback and UVB self-shielding treatment causes variance of flux PDF up to 5 – 10 per cent depending on the model, which is comparable to the jackknife errors, and so not too significant.

The simulated 1D Ly $\alpha$  power spectra show more intricate deviations from observations, and requires further analyses to understand them. Our Fiducial model captures the higher  $k$  modes well at  $\log(k [\text{s/km}]) > -1.3$  at  $z \sim 2.4$ , but at the same time underpredict the power at intermediate scales of  $\log(k [\text{s/km}]) \sim -1.5$ , and then overpredict at the large scales of  $\log(k [\text{s/km}]) < -2.5$ . This may have to do with the fact that we have not tuned our thermodynamic parameters (e.g., gas temperature) assuming the FGPA method. The NoFB and CW run results deviate from the Fiducial run only within  $1\sigma$  jackknife error, but the Shield and FG09 runs deviate from the Fiducial run more than  $1\sigma$ . The deviation is

the greatest for the FG09, probably due to the difference in the overall photoionization rate between the HM12 model adopted in the Fiducial run as we discussed in Section 3.2. In the future, we will further examine the 1D Ly $\alpha$  power spectra using higher resolution and larger box-size simulations.

Perhaps the more direct statistic is the flux contrast  $\eta_F$  as a function of impact parameter  $b$  from galaxies (Fig. 5). On large-scales of  $b > 1 h^{-1} \text{cMpc}$ , we find good agreement with observational estimates and the previous work by Sorini et al. (2018), which supports the correctness of the  $\Lambda$ CDM model and the large-scale structure that it predicts. On the other hand, on small scales, we find variations due to different parameters, such as the galaxy mass, probing depth, redshift, and feedback models. Overall our results show good agreement with currently available observations, however, we find an important dependence of  $\eta_F$  on galaxy stellar masses, where more massive galaxies are surrounded by more abundant HI gas with higher flux contrast. If one combines all the signals from all galaxies and average them over, then the stronger signal from more massive galaxies ( $M_{\star} \geq 10^{11} M_{\odot}$ ) is diluted by that of lower mass galaxies, and the flux contrast appears to be reduced in the proximity of galaxies.

We also see some ( $\sim 20 - 30\%$ ) variations in  $\eta_F$  on small scales depending on the physical treatment of feedback, self-shielding of gas, star formation, and UVB (Fig. 5e). It is somewhat counter-intuitive that the NoFB run has the lowest contrast, which is probably because much of the cold gas is consumed by star formation in the high-density galactic center. The CW run is the second lowest, owing to its efficient removal of gas from galactic potential with strong galactic wind. The Fiducial and the Shield model have about the same level of  $\eta_F$  on small scales. The FG09 run has the highest level of  $\eta_F$  relative to the HM12 model in the Fiducial run, perhaps due to its lower photoionization rate (see Section 3.2). While these deviations are interesting to discuss, the variation due to galaxy stellar mass and the probed path length ( $\delta_v$ ) is larger than that due to different feedback models. The redshift evolution of  $\eta_F$  is clearly seen, and the contrast at  $z \sim 3$  is higher than that at  $z \sim 2$  at all scales of  $100 \text{ ckpc} < b < 20 \text{ cMpc}$  due to higher  $\tau_{\text{eff}}$ . At the same time, we caution the reader that the results on  $\eta_F$  may not be fully converged due to its strong dependence on the box size and galaxy sample (see Appendix B).

We find a strong flux contrast around a proto-cluster at  $z \sim 2$  in our simulation, which is comparable to that for the galaxies with  $M_{\star} \geq 10^{10} - 10^{11} M_{\odot}$  (Fig. 12). This result certainly lends support for finding more

proto-clusters via HI tomography and massive galaxies associated with it.

The cross-correlation between galaxies and HI absorbers shows expected trends. For example, the higher EW sample is more correlated with galaxies than the lower EW sample, because more neutral HI gas is expected to be closer to the galaxies. More massive galaxies have stronger CCF signal on larger scales of  $> 500$  kpc, but the signal becomes noisy at smaller scales due to lack of correlating sample. The redshift evolution of CCF signal is not so strong, but we do see that it is stronger at  $z = 2$  than at  $z = 3$  at least on larger scales of  $> 1$  cMpc, as the cosmic structure develops and galaxy clustering becomes stronger. Our 2D CCF result (Fig. 9) shows the finger-of-god feature similarly to Turner et al. (2017), but it would require a transverse resolution of  $< 1$  cMpc resolution in the IGM tomography to study this effect in more detail observationally. Using our simulations, we intend to study the gas dynamics which causes these effects in more detail in our subsequent work, e.g., the impact of cold accretion flows and galactic outflows on the 2D CCF.

We also examined the correlation between galaxy overdensity  $\delta_{\text{gal}}$  vs. flux contrast  $\delta_F$ , and compared the results with those of Mukae et al. (2017) and Liang et al. (2021) using the same cylinder size as their measurements. Our simulation result shows a large scatter due to larger cylinder sample than in the observations, and a shallower best-fit slope than the observations (Fig. 10). These differences could be due to a few things, such as different galaxy sample used, cosmic variance, or photoionization effect by the radiation emitted by galaxies or quasars. This comparison study using the Mukae plot is not as definitive as the flux contrast at this point, however, it provides a support for such a methodology utilizing photo- $z$  galaxy sample that are more widely available with cheaper observational costs.

The examination of a protocluster in our simulation (Figs. 11, 12) also bring up interesting directions for our future research. In particular, we see a hot X-ray emitting gas in the center of the proto-cluster, but at the same time we don't see diffuse HI distribution near the center. Rather, it seems that the HI absorption is mostly contributed from individual galaxies rather than diffuse intra-protocluster medium, and when averaged over the spherical shells, it produces an enhancement of flux contrast in the central few 100 kpc. This result seems to be in line with that of Miller et al. (2019), in

the sense that the high- $\tau$  sightlines are dominated by galaxies and DLAs, while most of the sightlines simply have lower  $\tau$ . In our future work, we plan to follow up on these issues utilizing higher resolution zoom-in simulations of proto-clusters.

In this paper, we focused on the relative distribution of galaxies and HI, and did not touch on the metal absorption lines, which we will discuss in our future publications. The cross-correlation studies between galaxies, HI and metals will certainly give us useful information on the interplay between them and to learn more about star formation and feedback. The astrophysics in this subject is quite rich, and at the same time, quite challenging to get it all correctly, as we need to have a good understanding of cosmology, galaxy formation, star formation, feedback and chemical enrichment of the IGM, and link them all together to have a full picture.

We thank the anonymous referee for detailed comments which helped to improve the manuscript significantly. KN acknowledges useful discussions with J. X. Prochaska, and is grateful to Volker Springel for providing the original version of GADGET-3, on which the GADGET3-OSAKA code is based on. We also thank Yuri Oku for providing the L40N512 run for the comparison presented in the appendix. Our numerical simulations and analyses were carried out on the XC50 systems at the Center for Computational Astrophysics (CfCA) of the National Astronomical Observatory of Japan (NAOJ), OCTOPUS at the Cybermedia Center, Osaka University, and Oakforest-PACS at the University of Tokyo as part of the HPCI system Research Project (hp180063, hp190050, hp200041). This work is supported by the JSPS KAKENHI Grant Number JP17H01111 (KN), 19H05810 (KN), 20H00180 (KN, MO), JP18H05868 (KGL), and JP19K14755 (KGL). KN acknowledges the travel support from the Kavli IPMU, World Premier Research Center Initiative (WPI), where part of this work was conducted. The authors thank the developers of below software for making their code available on a free and open-source basis.

*Software:* CELib (Saitoh 2017), FFTW (<http://www.fftw.org/>), Grackle (Smith et al. 2017), GSL (Galassi 2009, <https://www.gnu.org/software/gsl/>), HDF5 (<https://portal.hdfgroup.org/>), Matplotlib (Hunter 2007), Numpy (Harris et al. 2020), SciPy (Virtanen et al. 2020)

## APPENDIX

## A. OBSERVATIONAL INFORMATION

In 2020s, we enter the era of massively multiplexed spectroscopy which enables us to study the IGM from small ( $\sim$  kpc) to large scales ( $\sim$  100 cMpc). This means that a unique era is coming soon where we can test the simulated universe by observations with a greater precision (i.e., the era of ‘*precision structure formation*’). In this appendix, to set the stage, we review some of the details of Subaru PFS and other near-future facilities. In particular, there is at the time of writing no published description of the planned PFS IGM tomography program, and so we will provide some details here.

## A.1. Subaru PFS (2023)

The Prime Focus Spectrograph (PFS; Sugai et al. 2015) is expected to be installed on the prime focus of Subaru Telescope in 2020–2021. Its wide field-of-view ( $1.25 \text{ deg}^2$ ) and large collecting area (8.2m in diameter) are unique among other facilities. There is continuous wavelength coverage is  $3800 \text{ \AA} - 1.26 \mu\text{m}$  with three cameras, at medium resolving power ( $R \equiv \lambda/\Delta\lambda \sim 2000 - 4000$ ). Currently, a large collaboration is planning to execute a survey with  $\sim$ 300 nights from 2023 through 2027, called the SSP (Subaru Strategic Program). This SSP is envisaged as having three components: the Cosmology Survey, Galactic Archeology Survey, and the Galaxy Evolution Survey — an early version of this SSP plan is outlined in Takada et al. (2014), although the details therein are no longer up-to-date.

The PFS Galaxy Evolution Survey, in particular, will be a deep survey covering approximately  $14 \text{ deg}^2$  across three of the Subaru Hyper Suprime Camera Deep imaging fields (Aihara et al. 2018). Across multiple visits, over 340,000 spectra will be obtained across multiple target classes ranging from  $0.7 \lesssim z \lesssim 7$ . One of the major goals of this project is to generate a 3-D tomographic map of the optically-thin HI at  $2.1 < z < 2.6$  with average transverse sight-line separation of  $\sim$  4 cMpc using 16,000 star-forming galaxies ( $g < 24.7$ ; see more details in Table A.1) at  $2.5 < z < 3.5$  acting as background probes of intervening absorbing neutral gas (i.e. IGM tomography). While this sightline density is similar to that of the CLAMATO Survey (Lee et al. 2018), the PFS program will be approximately  $50\times$  larger in area and volume, covering a combined comoving volume of  $4 \times 10^7 \text{ cMpc}^3$ . One of the primary products envisaged from these observations is the Wiener-filtered absorption maps of the large-scale structure traced by the diffuse Ly $\alpha$  forest, which will provide sufficient detail to recover the cosmic web on scales of  $\sim 4 h^{-1} \text{ Mpc}$  (Lee & White 2016; Krolewski et al. 2017). More recently, Horowitz et al. (2019) presented the TARDIS analysis framework which allows direct inference of the underlying density field, which allows reconstruction of smaller scale structures ( $\sim 2 h^{-1} \text{ Mpc}$ ) than Wiener filtering.

**Table 2.** Subaru PFS IGM Tomography Targets

Target Class	Redshift	Selection	Exposure	Targeted Objects	Number/PFS FOV
	Range		Time (hrs)	(Useful Spectra)	( $1.25 \text{ deg}^2$ )
IGM Background (bright)	2.5-3.5	$y < 24.3, g < 24.2$	6	8300 (5810)	690
IGM Background (faint)	2.5-3.5	$y < 24.3, 24.2 < g < 24.7$	12	14000 (9800)	1170
IGM Foreground	2.1-2.6	$y < 24.3$	6	22000 (15400)	1830

In addition to the LBGs and QSOs targeted as Ly $\alpha$  forest background sources, there will also be a category of ‘IGM Foreground’ galaxies selected to be at  $2.1 < z < 2.6$ , i.e., coeval with the Ly $\alpha$  absorption. This class of targets will be broadly selected among galaxies with  $y < 24.3$  (see Table A.1) to span a wide range of galaxy properties. Subaru PFS spectra should have sufficient spectral resolution and signal-to-noise

to measure the IGM metal absorption lines (e.g., Mg II, Si IV and C IV) simultaneously, as well as OII emission in the near-infrared. With approximately 15,000 useful spectra expected from this target class, we expect to be able to robustly test the trends discussed in this paper.

## B. BOX SIZE AND RESOLUTION TEST OF SIMULATIONS

In this section, we examine the effects of different box sizes and resolution for the Fiducial model on the basic statistics presented in this paper. The two simulations listed in Table 3, L50N256 and L100N512, have the same mass & spatial resolution but different box sizes, while the L40N512 has a higher resolution. In Fig. 13 we compare the flux PDF from three simulations at  $z = 3$  (just using a single snapshot of each simulation). The results of L50N256 and L100N512 overlap well within  $1\sigma$ , but L40N512 lies below the other two simulations at  $0.1 < F < 0.9$  by about  $1\sigma$  and higher at the lowest and highest  $F$  bins instead. Due to the higher resolution, the L40N512 run may have more optically-thick lines with  $F < 0.1$ , which instead pushes the PDF downward at  $F > 0.1$ . Note that the ordinate is in log-scale, therefore the differences at  $0.2 < F < 0.8$  is much smaller than those at  $F < 0.1$  and  $F > 0.9$ .

In Fig. 14, we compare the  $P_{1D}(k)$  from three simulations listed in Table 3. The three lines overlap well within  $1\sigma$  jackknife error at  $\log(k [\text{s}/\text{km}]) > -1.5$ . There is a bump at the intermediate range for L40N512 and L50N256 at  $\log(k [\text{s}/\text{km}]) \sim -1.3$  &  $-1.95$ , which could be due to the limited simulation volume used here for the test.

Figure 15 compares the flux contrast  $\eta_F$  for the same three simulations shown in Figs. 13 & 14. The results of L50N256 and L100N512 roughly agree within  $1\sigma$  at  $-1 \lesssim \log(b [\text{cMpc}]) \lesssim 0.5$ , but they deviate somewhat from each other at the smallest bin of  $\log(b [\text{cMpc}]) < -1.0$  and on larger scales of  $\log(b [\text{cMpc}]) \gtrsim 0.5$ . As the box size becomes smaller from L100 to L40,  $\eta_F$  converges

to zero at a smaller impact parameter, near the half of the simulation box size. The  $\eta_F$  of L40N512 is lower than the other two runs (except at the smallest bins of  $\log(b [\text{cMpc}]) \lesssim -1$ ), which cannot simply be explained by the box-size effect. With a higher resolution, L40 has a higher star formation rate density than L50 and L100 runs at all redshifts by about a factor of 2, which leads to more consumption of HI gas into stars and overproduction of lower mass galaxies in lower mass halos (because we didn't recalibrate the feedback parameters as the resolution was increased). This could result in less HI gas around the galaxies. In other words, the difference in resolution induces differences in the star formation rate and feedback (e.g., Meiksin et al. 2014, 2015), so the convergence test requires further detailed analyses on the star formation rates and galaxy populations which we plan to present in the future. The  $\eta_F$  of L40N512 and L50N256 agree at the smallest scale, but L100N512 result is higher than the former two runs at the innermost bin. This is because Fig. 15 was produced using only a single snapshot and the volume is limited, with limited number of massive galaxies with  $M_* > 10^{10} M_\odot$ . Therefore the L100N512 run with the largest number of massive galaxies is exhibiting the strongest  $\eta_F$  signal on small scales, here again showing the strong dependence of  $\eta_F$  on the galaxy stellar mass as we argued in Section 3.3 and Fig. 5(c),(d). Therefore we caution the reader that the results of  $\eta_F$  could depend on the box size and associated galaxy mass range strongly, and our results may not have fully converged yet. If we perform simulations with larger box sizes ( $L > 100 h^{-1} \text{Mpc}$ ), then the  $\eta_F$  signal might become even stronger with more massive galaxies in the simulated volume.

**Table 3.** Simulation Parameters

Simulations	Box Size	$N_{\text{ptcl}}$	$m_{\text{DM}}$	$m_{\text{gas}}$	$\epsilon_g$	$h_{\text{min}}$
	$[h^{-1} \text{cMpc}]$		$[h^{-1} M_\odot]$	$[h^{-1} M_\odot]$	$[h^{-1} \text{ckpc}]$	$[h^{-1} \text{pc}]$
L100N512 (Osaka20)	100	$2 \times 512^3$	$5.38 \times 10^8$	$1.00 \times 10^8$	7.8	260
L50N256	50	$2 \times 256^3$	$5.38 \times 10^8$	$1.00 \times 10^8$	7.8	260
L40N512	40	$2 \times 512^3$	$3.44 \times 10^7$	$6.43 \times 10^4$	2.6	87

NOTE—Parameters of the simulations used for resolution and box-size test. The L100N512 simulation corresponds to the Osaka20 runs listed in Table 1. The listed parameters are as follows:  $N_{\text{ptcl}}$  is the total number of particles (dark matter and gas),  $m_{\text{DM}}$  is the dark matter particle mass,  $m_{\text{gas}}$  is the initial mass of gas particle (which may change over time due to star formation and feedback),  $\epsilon_g$  is the comoving gravitational softening length, and  $h_{\text{min}}$  is the minimum physical gas smoothing length at  $z = 2$  (see Section 2.1).

## C. VARIATION IN $\eta_F$ DUE TO REDSHIFT OFFSET

Following the previous works (Font-Ribera et al. 2013; Prochaska et al. 2013; Meiksin et al. 2017), we examine

the impact of redshift errors of galaxies on  $\eta_F$  by introducing a Gaussian scatter in the galaxy redshift along

**Table 4.** Galaxy Counts

Simulations	$N_{\text{gal}}$			
	$10^8-10^9$	$10^9-10^{10}$	$10^{10}-10^{11}$	$>10^{11}M_{\odot}$
L100N512 (Osaka20)	8344	13893	3200	148
L50N256	1039	1705	425	14
L40N512	9476	3036	706	14

NOTE—Number of galaxies in each galaxy stellar mass range.

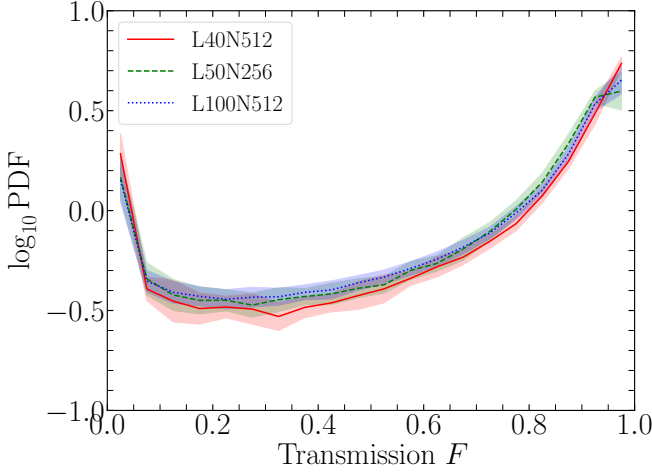


**Figure 13.** Flux PDF from the three simulations with different resolution and box sizes at  $z = 3$  (using a single snapshot of Fiducial model; see Table 3). The same number of bins as in Figs. 3c,d,e is used. The two simulations, L100N512 and L50N256 have the same mass & spatial resolution but with different box sizes, while the L40N512 has the highest resolution. See Table 3.

the LoS. Figure 16 shows the flux contrast with and without a Gaussian scatter of  $1\sigma = \pm 500 \text{ km s}^{-1}$  along the LoS for the galaxy redshifts. We find that the effect of redshift offset is not so strong, and only decreases the  $\eta_F$  signal by about 10 – 15 per cent. This is reasonable given that the velocity range of  $\delta_v = \pm 1000 \text{ km s}^{-1}$  is greater than the majority of Gaussian scatter.

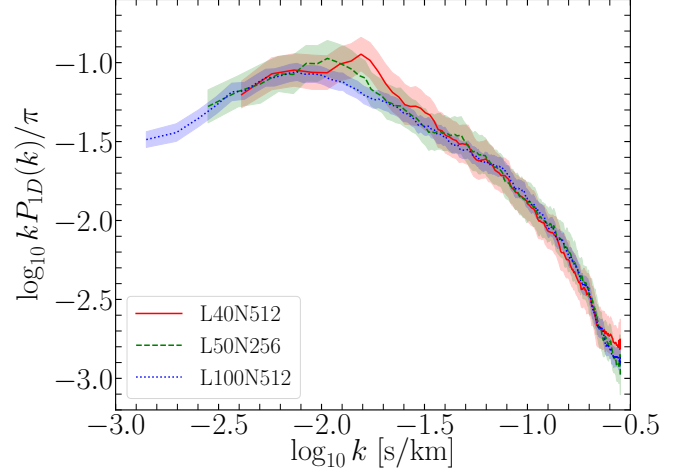


**Figure 14.** One dimensional power spectra from the three simulations with different resolution and box sizes at  $z = 3$  (see Table 3).

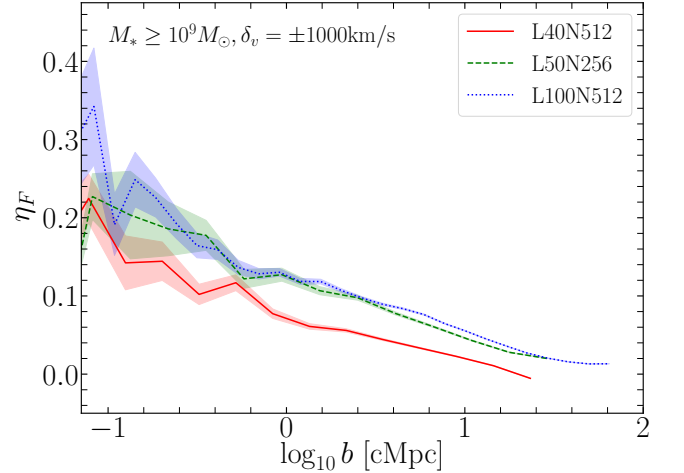


**Figure 15.** Flux contrast from the three simulations with different resolution and box sizes at  $z = 3$  (see Table 3).

## REFERENCES

- Ahn, C. P., Alexandroff, R., Allende Prieto, C., et al. 2012, *ApJS*, 203, 21
- Aihara, H., Arimoto, N., Armstrong, R., et al. 2018, *PASJ*, 70, S4
- Altay, G., Theuns, T., Schaye, J., Crighton, N. H. M., & Dalla Vecchia, C. 2011, *ApJL*, 737, L37
- Aoyama, S., Hou, K.-C., Shimizu, I., et al. 2017, *MNRAS*, 466, 105
- Bajtlik, S., Duncan, R. C., & Ostriker, J. P. 1988, *ApJ*, 327, 570
- Becker, G. D., Hewett, P. C., Worseck, G., & Prochaska, J. X. 2013, *MNRAS*, 430, 2067

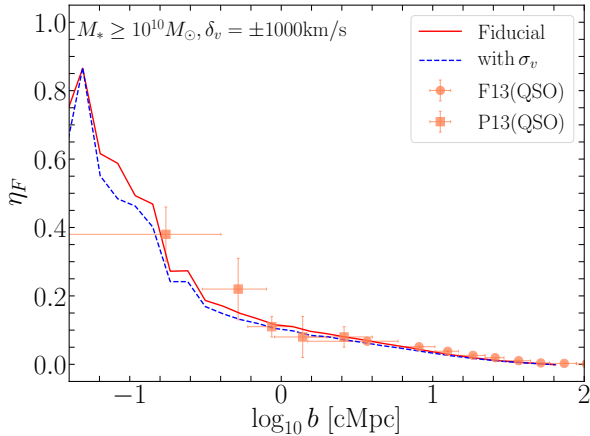


**Figure 16.** Flux contrast with and without a Gaussian scatter of  $\pm 500 \text{ km s}^{-1}$  along the LoS for the galaxy redshifts (blue dashed & red solid line, respectively). The red line is the same data as the one in Fig. 5(c) for  $M_* > 10^{10} M_\odot$  case.

Bergeron, J., Petitjean, P., Aracil, B., et al. 2004, *The Messenger*, 118, 40

Bird, S., Vogelsberger, M., Sijacki, D., et al. 2013, *MNRAS*, 429, 3341

Bolton, J. S., & Becker, G. D. 2009, *MNRAS*, 398, L26

Bolton, J. S., Puchwein, E., Sijacki, D., et al. 2017, *MNRAS*, 464, 897

Bruscoli, M., Ferrara, A., Marri, S., et al. 2003, *MNRAS*, 343, L41

Cai, Z., Fan, X., Peirani, S., et al. 2016, *ApJ*, 833, 135

Cai, Z., Fan, X., Bian, F., et al. 2017, *ApJ*, 839, 131

Calura, F., Tesconi, E., D’Odorico, V., et al. 2012, *MNRAS*, 422, 3019

Calverley, A. P., Becker, G. D., Haehnelt, M. G., & Bolton, J. S. 2011, *MNRAS*, 412, 2543

Cen, R., Miralda-Escudé, J., Ostriker, J. P., & Rauch, M. 1994, *ApJL*, 437, L9

Cen, R., Nagamine, K., & Ostriker, J. P. 2005, *ApJ*, 635, 86

Chabanier, S., Bournaud, F., Dubois, Y., et al. 2020, *MNRAS*, 495, 1825

Chabanier, S., Palanque-Delabrouille, N., Yèche, C., et al. 2019, *JCAP*, 2019, 017

Chevalier, R. A. 1974, *ApJ*, 188, 501

Chiang, Y.-K., Overzier, R. A., Gebhardt, K., & Henriques, B. 2017, *ApJL*, 844, L23

Choi, J.-H., & Nagamine, K. 2011, *MNRAS*, 410, 2579

Cirasuolo, M., Afonso, J., Carollo, M., et al. 2014, in *Society of Photo-Optical Instrumentation Engineers (SPIE) Conference Series*, Vol. 9147, Proc. SPIE, 91470N

Cowie, L. L., Songaila, A., Kim, T.-S., & Hu, E. M. 1995, *AJ*, 109, 1522

Crain, R. A., Theuns, T., Dalla Vecchia, C., et al. 2009, *MNRAS*, 399, 1773

Croft, R. A. C., Weinberg, D. H., Katz, N., & Hernquist, L. 1998, *ApJ*, 495, 44

Dalton, G., Trager, S. C., Abrams, D. C., et al. 2012, in *Society of Photo-Optical Instrumentation Engineers (SPIE) Conference Series*, Vol. 8446, Proc. SPIE, 84460P

Davé, R., Oppenheimer, B. D., Katz, N., Kollmeier, J. A., & Weinberg, D. H. 2010, *MNRAS*, 408, 2051

Dawson, K. S., Schlegel, D. J., Ahn, C. P., et al. 2013, *AJ*, 145, 10

Faucher-Giguère, C., Lidz, A., Zaldarriaga, M., & Hernquist, L. 2009, *ApJ*, 703, 1416

Font-Ribera, A., Miralda-Escudé, J., Arnau, E., et al. 2012, *JCAP*, 2012, 059

Font-Ribera, A., Arnau, E., Miralda-Escudé, J., et al. 2013, *JCAP*, 5, 018

Galassi, M. 2009, *GNU scientific library reference manual*, 3rd edn., Bristol : Network Theory Limited

Haardt, F., & Madau, P. 2012, *ApJ*, 746, 125

Harris, C. R., Millman, K. J., van der Walt, S. J., et al. 2020, *Nature*, 585, 357

Hernquist, L., Katz, N., Weinberg, D. H., & Miralda-Escudé, J. 1996, *ApJL*, 457, L51

Hopkins, P. F. 2013, *MNRAS*, 428, 2840

Horowitz, B., Lee, K.-G., White, M., Krolewski, A., & Ata, M. 2019, *ApJ*, 887, 61

Hunter, J. D. 2007, *Computing in Science & Engineering*, 9, 90

Iršič, V., Viel, M., Berg, T. A. M., et al. 2017, *MNRAS*, 466, 4332

Kim, J.-H., Abel, T., Agertz, O., et al. 2014, *ApJS*, 210, 14

Kim, J.-h., Agertz, O., Teyssier, R., et al. 2016, *ApJ*, 833, 202

Kim, T. S., Bolton, J. S., Viel, M., Haehnelt, M. G., & Carswell, R. F. 2007, *MNRAS*, 382, 1657

Kim, T. S., Viel, M., Haehnelt, M. G., Carswell, R. F., & Cristiani, S. 2004, *MNRAS*, 347, 355

Kollmeier, J. A., Miralda-Escudé, J., Cen, R., & Ostriker, J. P. 2006, *ApJ*, 638, 52

Kollmeier, J. A., Weinberg, D. H., Davé, R., & Katz, N. 2003, *ApJ*, 594, 75

Kriek, M., van Dokkum, P. G., Labbé, I., et al. 2009, *ApJ*, 700, 221

Krolewski, A., Lee, K.-G., Lukić, Z., & White, M. 2017, *ApJ*, 837, 31

Krolewski, A., Lee, K.-G., White, M., et al. 2018, *ApJ*, 861, 60

Lee, K.-G. 2012, *ApJ*, 753, 136

Lee, K.-G., & White, M. 2016, *ApJ*, 831, 181

- Lee, K.-G., Hennawi, J. F., Stark, C., et al. 2014, *ApJL*, 795, L12
- Lee, K.-G., Hennawi, J. F., White, M., et al. 2016, *ApJ*, 817, 160
- Lee, K.-G., Krolewski, A., White, M., et al. 2018, *ApJS*, 237, 31
- Liang, Y., Kashikawa, N., Cai, Z., et al. 2021, *ApJ*, 907, 3
- Lidz, A., Heitmann, K., Hui, L., et al. 2006, *ApJ*, 638, 27
- Lukić, Z., Stark, C. W., Nugent, P., et al. 2015, *MNRAS*, 446, 3697
- McDonald, P., Miralda-Escudé, J., Rauch, M., et al. 2000, *ApJ*, 543, 1
- McDonald, P., Seljak, U., Cen, R., et al. 2005, *ApJ*, 635, 761
- McDonald, P., Seljak, U., Burles, S., et al. 2006, *ApJS*, 163, 80
- McKee, C. F., & Ostriker, J. P. 1977, *ApJ*, 218, 148
- McQuinn, M. 2016, *ARA&A*, 54, 313
- Meiksin, A., Bolton, J. S., & Puchwein, E. 2017, *MNRAS*, 468, 1893
- Meiksin, A., Bolton, J. S., & Tittley, E. R. 2014, *MNRAS*, 445, 2462
- . 2015, *MNRAS*, 453, 899
- Meiksin, A., & White, M. 2004, *MNRAS*, 350, 1107
- Meiksin, A. A. 2009, *Reviews of Modern Physics*, 81, 1405
- Miller, J. S. A., Bolton, J. S., & Hatch, N. 2019, *MNRAS*, 489, 5381
- Miralda-Escudé, J., Cen, R., Ostriker, J. P., & Rauch, M. 1996, *ApJ*, 471, 582
- Momose, R., Shimizu, I., Nagamine, K., et al. 2020, *arXiv e-prints*, arXiv:2002.07334
- Momose, R., Shimasaku, K., Kashikawa, N., et al. 2021, *ApJ*, 909, 117
- Morris, J. P. 1996, *PASA*, 13, 97
- Mukae, S., Ouchi, M., Kakiichi, K., et al. 2017, *ApJ*, 835, 281
- Mukae, S., Ouchi, M., Cai, Z., et al. 2020, *ApJ*, 896, 45
- Muzzin, A., Marchesini, D., Stefanon, M., et al. 2013, *ApJS*, 206, 8
- Nagamine, K., Choi, J., & Yajima, H. 2010, *ApJL*, 725, L219
- Nagamine, K., Wolfe, A. M., Hernquist, L., & Springel, V. 2007, *ApJ*, 660, 945
- Overzier, R. A. 2016, *A&A Rv*, 24, 14
- Palanque-Delabrouille, N., Yèche, C., Borde, A., et al. 2013, *A&A*, 559, A85
- Palanque-Delabrouille, N., Yèche, C., Lesgourgues, J., et al. 2015, *JCAP*, 2015, 045
- Planck Collaboration, Ade, P. A. R., Aghanim, N., et al. 2016, *A&A*, 594, A13
- Prochaska, J. X., Hennawi, J. F., Lee, K.-G., et al. 2013, *ApJ*, 776, 136
- Rahmati, A., Pawlik, A. H., Raičević, M., & Schaye, J. 2013, *MNRAS*, 430, 2427
- Rahmati, A., Schaye, J., Bower, R. G., et al. 2015, *MNRAS*, 452, 2034
- Rakic, O., Schaye, J., Steidel, C. C., et al. 2013, *MNRAS*, 433, 3103
- Rakic, O., Schaye, J., Steidel, C. C., & Rudie, G. C. 2012, *ApJ*, 751, 94
- Rauch, M. 1998, *ARA&A*, 36, 267
- Ravoux, C., Armengaud, E., Walther, M., et al. 2020, *arXiv e-prints*, arXiv:2004.01448
- Rollinde, E., Theuns, T., Schaye, J., Pâris, I., & Petitjean, P. 2013, *MNRAS*, 428, 540
- Rubin, K. H. R., Hennawi, J. F., Prochaska, J. X., et al. 2015, *ApJ*, 808, 38
- Saitoh, T. R. 2017, *AJ*, 153, 85
- Saitoh, T. R., & Makino, J. 2009, *ApJL*, 697, L99
- . 2013, *ApJ*, 768, 44
- Schaye, J., Dalla Vecchia, C., Booth, C. M., et al. 2010, *MNRAS*, 402, 1536
- Scott, J., Bechtold, J., Dobrzycki, A., & Kulkarni, V. P. 2000, *The Astrophysical Journal Supplement Series*, 130, 67. <https://doi.org/10.1086/317340>
- Shimizu, I., Inoue, A. K., Okamoto, T., & Yoshida, N. 2014, *MNRAS*, 440, 731
- Shimizu, I., Todoroki, K., Yajima, H., & Nagamine, K. 2019, *MNRAS*, 484, 2632
- Smith, B. D., Bryan, G. L., Glover, S. C. O., et al. 2017, *MNRAS*, 466, 2217
- Sorini, D., Davé, R., & Anglés-Alcázar, D. 2020, *MNRAS*, 499, 2760
- Sorini, D., Oñorbe, J., Hennawi, J. F., & Lukić, Z. 2018, *ApJ*, 859, 125
- Sorini, D., Oñorbe, J., Lukić, Z., & Hennawi, J. F. 2016, *ApJ*, 827, 97
- Springel, V. 2005, *MNRAS*, 364, 1105
- Springel, V., & Hernquist, L. 2003, *MNRAS*, 339, 289
- Stinson, G., Seth, A., Katz, N., et al. 2006, *MNRAS*, 373, 1074
- Sugai, H., Tamura, N., Karoji, H., et al. 2015, *Journal of Astronomical Telescopes, Instruments, and Systems*, 1, 035001
- Takada, M., Ellis, R. S., Chiba, M., et al. 2014, *PASJ*, 66, R1
- Tasitsiomi, A. 2006, *ApJ*, 645, 792
- Tepper-García, T., Richter, P., & Schaye, J. 2013, *MNRAS*, 436, 2063
- Theuns, T., Viel, M., Kay, S., et al. 2002, *ApJL*, 578, L5

- Toshikawa, J., Kashikawa, N., Overzier, R., et al. 2016, *ApJ*, 826, 114
- Toshikawa, J., Uchiyama, H., Kashikawa, N., et al. 2017, *Publications of the Astronomical Society of Japan*, 70, 1708.09421
- Tumlinson, J., Peebles, M. S., & Werk, J. K. 2017, *ARA&A*, 55, 389
- Turner, M. L., Schaye, J., Crain, R. A., et al. 2017, *MNRAS*, 471, 690
- Turner, M. L., Schaye, J., Steidel, C. C., Rudie, G. C., & Strom, A. L. 2014, *MNRAS*, 445, 794
- Tytler, D., Paschos, P., Kirkman, D., Norman, M. L., & Jena, T. 2009, *MNRAS*, 393, 723
- Umehata, H., Tamura, Y., Kohno, K., et al. 2015, *ApJL*, 815, L8
- Umehata, H., Fumagalli, M., Smail, I., et al. 2019, *Science*, 366, 97
- Umehata, H., Smail, I., Swinbank, A. M., et al. 2020, *A&A*, 640, L8
- Viel, M., Becker, G. D., Bolton, J. S., & Haehnelt, M. G. 2013a, *PhRvD*, 88, 043502
- Viel, M., Lesgourgues, J., Haehnelt, M. G., Matarrese, S., & Riotto, A. 2005, *PhRvD*, 71, 063534
- . 2006, *Physical Review Letters*, 97, 071301
- Viel, M., Schaye, J., & Booth, C. M. 2013b, *MNRAS*, 429, 1734
- Virtanen, P., Gommers, R., Oliphant, T. E., et al. 2020, *Nature Methods*, 17, 261
- Walther, M., Hennawi, J. F., Hiss, H., et al. 2018, *ApJ*, 852, 22
- Weinberg, D. H., Katz, N., & Hernquist, L. 1998a, in *Astronomical Society of the Pacific Conference Series*, Vol. 148, *Origins*, ed. C. E. Woodward, J. M. Shull, & J. Thronson, Harley A., 21
- Weinberg, D. H., Burles, S., Croft, R. A. C., et al. 1998b, *ArXiv Astrophysics e-prints*, astro-ph/9810142
- Weymann, R. J., Carswell, R. F., & Smith, M. G. 1981, *ARA&A*, 19, 41
- Yajima, H., Choi, J.-H., & Nagamine, K. 2012, *MNRAS*, 427, 2889
- Yajima, H., Nagamine, K., Zhu, Q., Khochfar, S., & Dalla Vecchia, C. 2017, *ApJ*, 846, 30
- Zhang, Y., Anninos, P., Norman, M. L., & Meiksin, A. 1997, *ApJ*, 485, 496
- Zhang, Y., Meiksin, A., Anninos, P., & Norman, M. L. 1998, *ApJ*, 495, 63